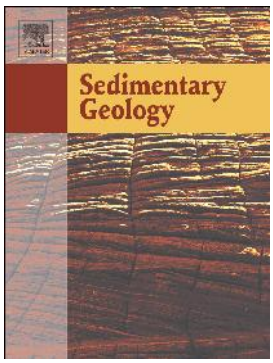

Tectonic controls on the Maastrichtian-Danian transgression in the Magallanes-Austral foreland basin (Chile): Implications for the growth of the Southern Patagonian Andes

Huber A. Rivera, Jacobus P. Le Roux, Marcelo Farías, Néstor M. Gutiérrez, Alejandro Sánchez, Sylvia Palma-Heldt

PII: S0037-0738(20)30060-9

DOI: https://doi.org/10.1016/j.sedgeo.2020.105645

Reference: SEDGEO 105645

To appear in: *Sedimentary Geology*

Received date: 24 January 2020

Revised date: 12 March 2020

Accepted date: 14 March 2020

Please cite this article as: H.A. Rivera, J.P. Le Roux, M. Farías, et al., Tectonic controls on the Maastrichtian-Danian transgression in the Magallanes-Austral foreland basin (Chile): Implications for the growth of the Southern Patagonian Andes, *Sedimentary Geology* (2020), https://doi.org/10.1016/j.sedgeo.2020.105645

Tectonic controls on the Maastrichtian-Danian transgression in the Magallanes-Austral foreland basin (Chile): implications for the growth of the Southern Patagonian Andes

Huber A. Rivera[1, 2, *], Jacobus P. Le Roux[1], Marcelo Farías[1], Néstor M. Gutiérrez[1], Alejandro Sánchez[3], Sylvia Palma-Heldt[4]

[1]Departamento de Geología, FCFM, Universidad de Chile, Plaza Ercilla 803, Santiago, Chile

[2]Université Grenoble Alpes, Université Savoie Mont Blanc, CNRS, IRD, IFSTTAR, ISTerre, 38000 Grenoble, France [3]Departamento de Ingeniería en Minas, Universidad de Santiago de Chile, Av. O'Higgins 3363, Estación Central, Santiago, Chile

[4]Departamento de Ciencias de la Tierra, Universidad de Concepción, Barrio Universitario S/N°, Concepción, Chile

***Corresponding author:** riverarh@univ-grenoble-alpes.fr; huber.rivera@ug.uchile.cl

ABSTRACT

The Maastrichtian-Danian transgression was one of the most extensive Atlantic-derived marine incursions in Patagonia. This study examines its stratigraphic record and origin in the Magallanes-Austral Basin, revealing an interplay of sedimentation, tectonism, and base-level changes, which contribute to our understanding of foreland basin dynamics. We present a multidisciplinary approach from a relatively poorly documented sector (51°38'-53°50'S) of the basin. This approach includes facies and provenance analysis, palynology, sequence stratigraphy, and U-Pb geochronology. These techniques enable us to evaluate the role of climate, tectonics, and eustasy on the transgression, as well as providing insight into the growth of the Southern Patagonian Andes. A first shallowing-upward cycle (late Campanian to late Maastrichtian) is represented by the transition from outer shelf and upper slope deposits (Fuentes and Tres Pasos formations) to shoreface and deltaic environments (Rocallosa and Dorotea formations), favoured by high erosion rates in the fold-thrust belt and eustatic sea-level drop. A subsequent deepening-upward cycle (late Maastrichtian to Paleocene) records the Atlantic transgression, manifested by estuarine deposits in an incised valley (uppermost Dorotea Formation) and deep-water turbidites (Chorrillo Chico Formation and Cabo Naríz beds). Palynological results suggest a temperate palaeoclimate (~6-17°C) during the Maastrichtian-Danian,

which agrees with significant cooling of the South Atlantic Ocean at this time. Therefore, relative climatic optima are not a driver of marine ingression. The stratigraphic and tectonic evolution of the succession studied suggests that flexural and dynamic subsidence promoted marine incursion into the Magallanes-Austral Basin. Provenance data indicate sediment input to the basin from the Southern Patagonian Batholith, Rocas Verdes Basin remnants, Tobífera Formation, and metamorphic terranes exposed in the hinterland of the Southern Patagonian Andes during the early Maastrichtian. However, by the Paleocene, sediments derived from the hinterland had been structurally dammed during basinward propagation of the fold-thrust belt.

Keywords: Cretaceous palaeoclimate; Provenance analysis; Southern Patagonian Andes; Sequence stratigraphy; U-Pb geochronology.

1. INTRODUCTION

In foreland basins, transgressive events are considered as an essential tool for understanding tectonic evolution due to their common link with thrusting events (e.g., Kamola and Huntoon, 1995; Hernández et al., 2005; Rodazz et al., 2010; Aguirre-Urreta et al., 2011; Gianni et al., 2018). Furthermore, transgressive deposits have provided valuable insights into the balance among supra- and sub-crustal static loading and unloading phases, sedimentation, and subsidence in the complex and dynamic evolution of foreland basins (Cross and Pilger, 1978; Catuneanu et al., 1997; Catuneanu, 2004; Hernández et al., 2005; Yang and Miall, 2008; Rodazz et al., 2010).

In Patagonia, the Maastrichtian-Danian transgression is considered to have been the most extensive (34°S-54°S) Atlantic-derived marine ingression (i.e., without the influence of Pacific ocean waters) that affected most of Patagonian basins (Náñez and Malumián, 2008; Malumián and Náñez, 2011; del Río and Martínez, 2015) (Fig. 1a). However, the origin of the Maastrichtian-Danian transgression is still controversial. Previous interpretations range from eustatic effects linked with warm-climatic episodes (Náñez and Malumián, 2008; Malumián and Náñez, 2011; Vallekoop et al.,

2017) to purely tectonic causes (Aguirre-Urreta et al., 2011; Giani et al., 2018), or a combination of both (Uliana and Biddle, 1988; Guler et al., 2019). A eustatic cause alone is unlikely, however, because the Maastrichtian-Danian transgression occurred during a period of cooling in the South Atlantic, indicated by $\delta^{18}O$ records of planktic and benthic foraminifera (Barrera and Savin, 1999; Cramer et al., 2009; Le Roux et al., 2012) (Fig. 1b). Moreover, between the Campanian and Selandian, a gradual eustatic sea-level fall is apparent (Haq, 2014) (Fig. 1b), which may suggest a potential link to tectonically-induced subsidence.

The palaeontological record of the Maastrichtian-Danian transgression has been exhaustively studied over the past 20 years throughout Patagonia (e.g., Malumián and Caramés, 1997; Náñez and Malumián, 2008; Malumián and Náñez, 2011; Aguirre-Urreta et al., 2011; del Río and Martínez, 2015; Vallekoop et al., 2017; Guler et al., 2019). In contrast, few studies deal with the sedimentological record, and most of these were focused on the northernmost basins (Neuquen Basin: Barrio, 1990; Aguirre-Urreta et al., 2011; Cañadón Asfalto Basin: Scasso et al., 2012). In the Magallanes-Austral Basin (MAB; Fig. 1a), *Corysphostoma incrassate*-bearing sandstones and glauconitic-rich facies have been traditionally related to the transgression (Malumián and Caramés, 1997; Mpodozis et al., 2011). However, these proposals, based on foraminifera or glauconitic content, were not backed up by systematic facies analysis. In the northern sectors of the MAB, the transition of non-marine to marine deposits facilitated recognition of the flooding event and allowed sedimentological studies in greater detail than previously achieved (e.g., Marenssi et al., 2004; Odino et al., 2018). Nevertheless, the sedimentological record of the transgression remains poorly studied in most of the central and southern parts of the basin.

This study presents a detailed sedimentological and sequence stratigraphic analysis, palynological data, and ~400 new detrital zircon U-Pb geochronological ages from a relatively poorly known sector (51°38'-53°50'S; Fig. 2a) of the MAB. Our work aims to amplify the current

knowledge of the stratigraphic and sedimentological record of the Maastrichtian-Danian Atlantic transgression and contribute to the growing body of knowledge regarding the variability of transgressive deposits by characterising both vertical and lateral facies changes, sequence stratigraphic architecture, and sedimentary provenance. This approach also allows us to provides a stratigraphic sequence framework that: (1) facilitates the identification of the transgressive deposits within a context of continuous marine sedimentation, and (2) develops an understanding of the juxtaposition, evolution, and inter-basin correlation of the depositional units (from Campanian-Maastrichtian to Paleocene). This enables us to evaluate to what extent climate, eustasy and tectonics controlled the marine incursion into the MAB. Finally, we discuss the causative mechanisms on a broad regional scale. Our provenance results combined with the conclusions of previous studies, constrain the timing of the latest Cretaceous to early Cenozoic tectonic events and shed light on the building phases of the Southern Patagonian Andes.

2. TECTONIC AND STRATIGRAPHIC SETTING

The MAB (Fig. 1a) is a retroarc foreland basin (Biddle et al., 1986; Wilson, 1991) resulting from the closure of the extensional Rocas Verdes Basin (RVB) in the mid- to late Cretaceous (112-86 Ma) (Fildani et al., 2003; Klepeis et al., 2010; Fosdick et al., 2011; McAtamney et al., 2012). The MAB is oriented subparallel to the Jurassic-Neogene Southern Patagonian Batholith (Hervé et al., 2007). These plutonic rocks intruded low- to high-grade metamorphic rocks of the late Devonian-Permian Andean metamorphic complex (Hervé et al., 2003), the Ordovician-Permian Darwin Cordillera (Barbeau et al., 2009; Hervé et al., 2010), and Middle Jurassic-Early Cretaceous volcaniclastic to metavolcanic rocks of the Tobífera-Lemaire-El Quemado formations (Wilson, 1991; Pankhurst et al., 2000; Calderón et al., 2007; Malkowski et al., 2016). The fold-thrust belt that bounds the MAB to the west (Fig. 1a) exposes remnants of the Upper Jurassic-Lower Cretaceous (154-100 Ma) siliceous, argillaceous, volcaniclastic, and ophiolitic rocks of the extensional RVB (Dalziel, 1981; Fildani and Hessler, 2005; Calderón et al., 2007), as well as metamorphic basement

and clastic deposits of the exhumed foreland basin strata (Fig. 1a). Together, the terranes described above constitute potential sediment sources for the strata studied here.

2.1 Stratigraphic overview of the study area

Our study encompasses the uppermost Fuentes, Rocallosa, Dorotea, and Chorrillo Chico formations, representing the late Campanian to Thanetian (Fig. 1b). The Fuentes Formation (Campanian) is a shale-dominated succession with thin sandstone intercalations, overlain by the Rocallosa Formation (Maastrichtian-Danian?) characterised by fine-to-coarse-grained, argillaceous, glauconitic sandstones, which in turn are overlain by the Chorrillo Chico Formation (Paleocene) composed of bathyal shales, siltstones, and clay-rich glauconitic sandstones (Thomas, 1949; Charrier and Lahsen, 1969; McDonnald, 1986; Álvarez et al., 2006; Mpodozis et al., 2011). The latter formations were studied along the northern coast of the Skyring Sound, Riesco Island (Fig. 2a, c), and Brunswick Peninsula (Fig. 2a, d) within the Magallanes Province of Chile (Fig. 2a). The Dorotea Formation (latest Campanian to Selandian) is a sandstone-dominated unit intercalated with conglomerates and mudstones, with southward-directed clinoforms representing a shelf-edge deltaic system (Covault et al., 2009; Schwartz and Graham, 2015; Gutiérrez et al., 2017; Manríquez et al., 2019). The Dorotea Formation was studied at Cerro Pelario, the Demaistre locality, as well as the southern extension of Sierra Dorotea within the Última Esperanza Province of Chile (Fig. 2a, b). Additionally, we present new petrological data of the turbidite deposits of the Cabo Naríz beds (equivalent to the Chorrillo Chico Formation) studied previously by Sánchez et al. (2010) along the west coast of Tierra del Fuego (Fig. 2a). This strategic distribution of stratigraphic sections (Table 1, Fig. 2a) allows us to study in greater detail the facies changes and depositional evolution along the axis of the basin, particularly in a poorly-known portion of the MAB. In Argentina, the Maastrichtian-Danian deposits are referred to as the Calafate Formation (Fig. 1b) around the Lago Argentino, north of our study area (Fig. 2a), and as the Monte Chico and Cerro Dorotea formations (Fig. 1b) in the Rio Turbio area, to the east of our study area in the Última Esperanza Province (Fig.

2a). South of our study area, in Tierra del Fuego (Fig. 2a), the Maastrichtian-Danian is represented by the Cerro Cuchilla Formation-Cabo Nariz beds (Fig. 1b) (within the Chilean part), and Policarpo Formation (Fig. 1b) (within the Argentinian part) (Olivero et al., 2003; Sánchez et al., 2010).

2.2 Tectonic events in the fold-thrust belt

During the Maastrichtian-Danian transgression, a deformational pulse that took place in the Southern Patagonian Andes may have been one of the primary drivers of transgression in the MAB. In the Ultima Esperanza Province, it is inferred by the Tenerife thrusting (with a basal décollement on the argillaceous Zapata Formation) between 74-27 Ma (Fosdick et al., 2011), which continued exhuming the Tobífera Formation and incorporated Upper Cretaceous foredeep deposits into the fold-thrust belt. In the Magallanes Province, Betka et al. (2015) suggested a phase of out-of-sequence thrusting and basement-involved reverse faulting beginning in the Maastrichtian and extending to the Paleogene. The deformation and cooling ages of ophiolitic blocks in the hinterland around 74-72 Ma (Rapalini et al., 2008) together with progradation and depositional system shoaling (Tres Pasos and Dorotea formations) (Covault et al., 2009; Romans et al., 2009; Schwartz and Graham, 2015; Schwartz et al., 2017; Gutiérrez et al., 2017) may also reflect deformation in the fold-thrust belt. In Tierra del Fuego, brittle-ductile deformation in the internal thrust-belt took place between ~72-64 Ma ("D1" contraction event; see Torres-Carbonell et al., 2013) concomitant with an uplift in the Cordillera Darwin Complex (Kohn et al., 1995).

3. METHODS

We measured nine stratigraphic columns (some composite; Table 1, Fig. 3) totalling ~1500 m, using a Jacob staff and tape measure on the best available exposures, which led us to recognise facies associations comprised by some sub-facies associations. Palaeocurrent measurements were taken mainly from trough axes (i.e., 3D trough cross-lamination/stratification, and 3D rib and furrow structures), planar cross-lamination, ripple marks, flute casts, current-oriented wood or tree trunks, and tool marks. The transport direction of the latter two bidirectional structures was usually resolved

considering other unidirectional structures nearby. Bioturbation variability was expressed in terms of the Bioturbation Index (BI; after Bann et al., 2004), which is a semi-quantitative estimate of the intensity of biogenic structures based on observations in two-dimensional, vertical to sub-vertical exposures. Additional sedimentological information can be found in Appendix A.

We used a model-independent approach for the sequence stratigraphic analysis (Catuneanu et al., 2011). Our objectives were to (1) highlight changes in basin accommodation on a regional scale; (2) provide a better understanding of the interplay between the depositional elements in time and space; and (3) allow the integration of diverse local stratigraphic architectures among the different sectors of the basin. Recognition of surfaces of sequence stratigraphic significance, stratal stacking patterns in outcrops, and their correlation among the different parts of the study area are mainly based on changes in accommodation-sedimentation dynamics and vertical relationships among the sedimentary environments.

Fine- to medium-grained sandstone samples were used preferentially for petrographic point-counting (n=27), detrital zircon uranium-lead (U-Pb) geochronology (n=4), and palynological analysis (n=3). For sandstone modal analysis, we conducted thin section point counts of 310 to 500 grains by using the Gazzi-Dickinson method (Ingersoll et al., 1984). Modal compositions were then normalised to quartz-feldspar-lithic (QFL) and monocrystalline quartz-feldspar-total lithic (Q_mFL_t) ternary plots to be compared with the tectonic fields of Dickinson (1985). The raw point-counting results are presented in Appendix B.

Detrital zircon U-Pb ages were used to assess provenance, as well as to calculate maximum depositional ages of the studied units. Samples RB1 and PB1 were collected from the lower part of the Chorrillo Chico Formation (Figs. 2d, 3a). In contrast, samples ZPR1 and ZLP1 correspond to the lower and upper parts of the Rocallosa Formation (Figs. 2b, c, 3a, b) respectively. Sample RB1 (n=54) was analysed using LA-MC-ICP-MS at the Mass Spectrometry Laboratory (CEGA) of the University of Chile. Samples ZPR1 (n=79) and ZLP1 (n=83) were analysed using LA-ICP-MS at the

Laboratory of Isotopic Studies of the Geosciences Centre, Mexico (UNAM). Sample PB1 (n=63) was analysed at the Geochronology Laboratory of SERNAGEOMIN by using LA-ICP-MS. To determine maximum depositional ages of individual sandstone samples, we calculated the weighted mean age of the youngest peak (≥ 2 grains within a 2σ-level error overlap; after Dickinson and Gehrels, 2009; Schwartz et al., 2017) of the age spectrum. We report each age with its mean square weighted deviation (MSWD) and the associated range of acceptable MSWDs based on the number of analyses contributing to each calculation (after Mahon, 1996). The number of detrital zircons analysed by formation (at least 117) helped to ensure that no fraction ≥ 0.05 was missed with a 95% confidence level (Vermeesch, 2004). Therefore, there is a good representation of all populations to interpret provenance. Likewise, when we considered the number of grains analysed per sample (to calculate a maximum depositional age), there was a 95% chance of finding at least three grains from every population that makes up ≥ 7% of the total zircon content (Rossignol et al., 2019). A detailed description of the separation, analytical and statistical technique, as well as raw histograms and Concordia plots for detrital zircon analyses, can be found in Appendix C. The detrital zircon U-Pb geochronological analyses are shown in Appendix D.

We selected fine-grained sandstone samples from the Rocallosa Formation for palynomorph identification. Approximately 5 g of each sample was crushed and oven-dried (60°C), after which the samples were treated with 10% HCl, HNO_3, and 40% HF to dissolve carbonate and silica minerals before the acetolysis process; the residues were mounted in glycerin jelly for observation under an Olympus CH/30 microscope and photographing using an Olympus CX 31 301 camera. All slides are presently housed in the Laboratory of Paleopalynology of the Departamento de Ciencias de la Tierra, Universidad de Concepción, under the codes 1525, 1526, and 1527. We inferred temperature data, and the climate type for each identified terrestrial palynomorph identified based on its botanical affinity with the nearest living relatives, assuming little evolutionary change in morphology or habitat preference for each taxon. However, care must be taken with these inferences since a single

fossil taxon could be affiliated with one or several modern families with different ecological tolerances, or it could have been affected in the past by allogenic factors that influenced the vegetational composition (for further details about climatic and ecological interpretation cautions see Bowman et al., 2014).

4. RESULTS AND INTERPRETATIONS

4.1 SEDIMENTOLOGY

We recognised nine facies associations (FA) (see facies synthesis in Table 2) which were described in stratigraphic order, i.e., from the Fuentes to Chorrillo Chico formations. We measured a total of 238 palaeocurrents, of which 86 are from the Cabo Naríz beds. The section location, outcrop photos and additional sedimentary and biogenic structure images are provided in Appendix A.

4.1.1 Fuentes Formation

The upper part of the Fuentes Formation comprises FA1 and FA2 (Fig. 3a) in section BH (Table 1, Fig. 2d). FA1 consists of thin intercalations of laminated shales (Fh), and massive to vaguely laminated siltstones and sandstones (Slm, Sm). Some tabular mudstone (Fm) intervals are also present, which reach up to tens of meters in thickness (Fig. A1a). Occasionally, units grade internally in cycles typically about 15 cm thick. Slump structures (Fig. 4a), tool marks at the bases of Sm facies, and laterally continuous contorted marlstone beds were also observed. FA2 occurs in the uppermost part of the unit (Fig. 3a), underlying the Rocallosa Formation. FA2 (Fig. A1b) is characterised by tabular Fm and Fh facies that rapidly grade upward into well-stratified siltstones (Slh), massive, fine-grained sandstones (Sm) with tool marks at the base, fine-to-medium-grained sandstones with hummocky cross-stratification (Shcs) and planar, low-angle cross lamination (Spl) commonly showing some wave ripple-lamination (Sw) that is slightly contorted at the tops of units. The glauconite content is ~5% in the mudstone and ~30% in the sandstone facies. In Fh and Fm facies, the bioturbation is low to moderate (BI 0-3). In Fh, bioturbation is characterised by abundant *Stelloglyphus llicoensis* (Fig. A1.1), *Chondrites* isp., *Phycosiphon incertum* ?, *Planolites* isp., and

rare *Rhizocorallium* isp., and *Bergaueria* isp. In Fm, bioturbation is characterised by *Phycodes* isp. (Fig. A1.2), *Palaeophycos* isp., *Cladichnus* cf. *fischeri* (Fig. A1.3) and *Phoebichnus bosoensis* (Fig. A.1.4). The Sm and Slm facies are slightly more bioturbated (BI 1-4) with trace fossils confined to the bedding planes, containing *Palaeophycus* isp., *Planolites* isp., *Chondrites* isp., *Zoophycos* isp., *Thalassinoides* isp., *Cylindrichnus* isp., *Teichichnus* isp. (Fig. A1.5) and undetermined trace fossils. Bidirectional palaeocurrent indicators suggest west to east flows.

The fine-grained nature of FA1 and degree of bioturbation related to the *Zoophycos* ichnofacies suggest a low-energy and open marine environment below storm-wave base (Bann and Fielding, 2004; Buatois and Mángano, 2011). The thick mudstone facies (Fm) and internally graded units (Fh and Sm) reflect settling of hemipelagic mud and deposition by mud-rich, low-density turbidity currents (Shultz et al., 2005; Romans et al., 2009; Malkowski et al., 2017a) in an outer shelf setting, as supported by the slump and contorted structures, as well as the abundant presence of *Stelloglyphus llicoensis* commonly found in this kind of environments (Le Roux et al., 2008). The relative abundance of silt and sand grain sizes, as well as storm- (Shcs) and wave-generated (Sw) structures in FA2, indicate that the depositional setting was shallower than that of FA1, above storm wave base and close to fair-weather wave base (Rossi and Steel, 2016). However, the trace fossil assemblage still indicates a fully marine environment. These turbidite/tempestite events favoured the colonisation of opportunistic organisms, a mechanism that has proved to be effective to provide higher oxygenation and nutrients to an otherwise poorly oxygenated setting (Rivera et al., 2018). The Shcs and Spl facies suggest the influence of strong oscillatory or combined flows, whereas the associated symmetrical ripples (Sw) indicate the waning phases of storm-related events (Dott and Bourgeois, 1982). The action of subsequent surge flows can explain the slightly contorted wave ripple tops. Those flows developed high shear stress and liquefied the previously deposited beds. Alternatively, contorted wave ripple tops could also have resulted from gravity-driven instability acting on unconsolidated water-saturated sediments (McDonald, 1986; Myrow et al., 2002). FA2

represents sedimentation in a phase of progradation from an offshore to lower shoreface environment.

4.1.2 Rocallosa Formation

Most of the Rocallosa Formation in sections BH, PR, PE, and PP (Table 1, Fig. 2c, d) is dominated by FA3, while its upper member is mainly composed of FA4. FA2 is locally present (Fig. 3a). FA3 comprises a crudely coarsening- and thickening-upward succession of up to 70 m thick and consists of wispy and planar laminated siltstones (Slh), vaguely stratified, massive siltstones (Slm), well-stratified and massive, bioturbated, fine-grained sandstones (Sm) internally showing crude normally graded beds up to 10 cm thick. Locally, hummocky cross-stratified sandstone beds (Shcs) with pebbly sandstones on their erosive bases are associated with wave-rippled beds (Sw). Glauconite is present throughout FA3 (~35-42%), and the bioturbation is variable (BI 1-4), being characterised by *Zoophycos* isp., *Chondrites* isp., *Planolites* isp., *Teichichnus* isp. (Fig. A1.6), and *Palaeophycus* isp. FA4 is composed mostly of well-sorted, fine-to-coarse-grained sandstones showing Shcs facies at the base and convolute (Fig. A1c) or wave ripple lamination (Sw) on bed tops, together with trough cross-bedding (St; sometimes diffuse), and planar- and low-angle cross-stratification (Spl). Additionally, well-sorted, medium-grained sandstone with low-angle cross-lamination and planar lamination (Spl; up to 1 m thick) and scour-and-fill structures are present. The scours are covered by medium-to-coarse pebbles of quartz, andesite, and reworked glauconite. In some intervals, Sm and Slh facies are intercalated. Locally, angular to sub-angular pebbles and cobbles (up to 7 cm in diameter) composed of glauconite, quartz, and lithic fragments (see Fig. 5a) are dispersed in the sandstone beds. Bioturbation is low to absent (BI 0-1). Palaeocurrent indicators are highly variable with modes towards the ENW and ESE.

The characteristic well-developed stratification, symmetrical ripples, wispy lamination and abundant trace fossil assemblage of *Cruziana* ichnofacies in FA3, suggest a wave-dominated open marine environment (Bann and Fielding, 2004; Buatois and Mángano, 2011) where sedimentation

mechanisms were similar to FA2. The association of erosive-based HCS beds and wave-rippled sandstones suggest episodic high-energy storm events in which strong unidirectional and oscillatory processes were active (e.g., Malkowski et al., 2016). These scours represent offshore-directed rip currents during storm events. According to its stratigraphic position and the interplay with adjacent facies associations, we interpret FA3 to represent a lower to middle shoreface. The presence of St and Spl facies on well-sorted sediments in FA4 reflects accumulation in longshore runnels and ridges within the high-energy surf and breaker zone above fair-weather wave base. Hummocky cross-bedding grading upward to wave-rippled beds suggest progressive waning of the large-scale oscillatory flows (storm events) (Dumas and Arnott, 2006; Malkowski et al., 2016). FA4 is interpreted as a mid-to-upper shoreface environment. However, the angular to sub-angular pebbles and cobbles dispersed in scoured, coarse-grained sandstones associated with wave-generated structures and low-angle to planar lamination, are interpreted as the transition to a foreshore-beach environment subject to swash processes caused by breaking waves.

4.1.3 Dorotea Formation

The Dorotea Formation includes FA2-8 (Fig. 3b). In sections DM and CP (Table 1, Fig. 2b) it presents facies (FA3-4) comparable with the Rocallosa Formation (studied farther south) as described above. However, amalgamated hummocky- and swaley cross-stratification (Shcs; Fig. 4b) is more abundant in FA4 of the Dorotea Formation, where pervasive bioturbation (BI 4-6) is present, as reflected by the massive, fuzzy and reworked textures in some intervals. In section CP, FA7 (Fig. 3b) comprises prominent lenticular to channeliform morphological ridges (Fig. A1h) ranging from 44-140 m long (along strike) and 5-26 m thick, enclosed in interbedded wavy laminated, very fine-grained sandstones and siltstones (Sw) (poorly exposed by vegetation) of FA3-4. FA7 is erosionally based and, composed of poorly selected, matrix-supported, massive to normally graded conglomerate (Gmm, Gmg) (rarely showing bedding planes) where large sub-angular clasts (up to 1 m in diameter; Fig. 4d) are composed entirely of massive sandstones and greenish mudstones. Sub-rounded, coarse

pebbles correspond to basalt (70%), andesite (20%), and chert (10%); shell hash and carbonaceous fragments are dispersed throughout the FA7. In addition, there are massive and trough cross-stratified, medium-grained sandstone packages (Sm, St), and fining-upward successions with rip-up clasts (or shell lag mantling a scoured surface; Fig. 4e, f) at the bases, as well as rippled sandstones (Sr), laminated sandstones and siltstones (Spl, Slh) with abundant organic matter and carbonised trunks and pedogenic features in some layers. Bioturbation in FA7 is rare to absent. Overlying FA7 there is a ~90 m thick succession of fine-grained sandstones intercalated with some mafic sills exposed in a vertical cliff, which precludes their detailed study.

In section SD (Figs. 2b, 3b), the base to the middle part of the formation is arranged in a series of coarsening-upward packages ranging from 15 m to 100 m thick (Fig. 3b). From base to top, the basal packages consist of FA5, FA6 and rarely FA4 on top; those of the middle part of the formation consist of FA5 (or rarely FA2), FA3, and FA4 on top (Fig. 3b). FA4 differs slightly from that previously described in presenting abundant carbonaceous material and shell hash, and in some intervals, it is possible to observe a transition from hummocky- to swaley cross-stratification (Fig. 4c). FA5 (Fig. A1d) is characterised by 1-6 m thick Fh and Fm facies, intercalated with sharp-based and tabular, Slm and Sm beds up to 50 cm thick. In a few cases, the muddy deposits are separated by 60 cm thick, tabular, very fine-grained sandstones with hummocky cross-stratification (Shcs). The bioturbation is mild (BI 0-2) characterised by *Chondrites* isp., *Zoophycus* isp., *Teichichnus* isp., *Planolites* isp., and *Taenidium* isp. and is distributed in the mudrock intervals. FA6 is divided into three sub-facies associations. FA6a is composed of lower regime planar-laminated, fine-to-medium-grained sandstones (Spl) with St, and Sm facies. Some intercalations consist of massive siltstone beds (Slm), coarse-grained lenses, scour surfaces (filled with hummocky cross-stratification or Spl facies; Fig. A1e) and carbonaceous plant debris. Some *Turritela* sp. and fragmented shells are present. Bioturbation is moderate (BI 1-4) and restricted to the Sm facies, which consists of *Thalassinoides* isp., *Chondrites* isp., *Taenidium* isp., *Asterosoma* isp., and *Ophiomorpha* isp. FA6b

includes 2-4 m thick packages of Sm facies, and medium-grained sandstones with dune-scale (sets of ~10 m wavelength and 1 m high) trough cross-bedding (St) (Fig. A1f) frequently associated with scour-and-fill structures filled with coarse to gritty sandstones. Bioturbation is mild (BI 1-2) and represented by *Macaronichnus* isp. (Fig. A1.7), *Planolites* isp., and *Diplocraterion*? isp. FA6c is arranged in fining-upward successions of up to 8 m thick, which comprise normally graded, very coarse to (upper) medium-grained sandstones (Sm) with scoured bases and rip-up clasts, followed by medium-grained, planar or trough cross-bedded sandstones (Spa, St) with some muddy partings. Bioturbation is low (BI 0-1), being restricted to *Schaubcylindrichnus* isp. (Fig. A1.8).

The upper part of the Dorotea Formation, in section SD, presents FA7 and FA8 (Fig. 3b). FA7 consists of 1-10 m thick, tabular to lenticular, fining-upward sandstones units. At the base, erosion surfaces covered with pebble and/or shell lag are followed by medium-grained, massive or high-angle planar cross-laminated sandstones (Spa, Sm) that in turn grade upward into mottled, fine- to very fine-grained sandstone with ripple remnants (Sr), Spl facies, and plant remains or carbonised wood at the top. Commonly, bed tops are sharp or wavy. FA8 is divided into three sub-facies associations. FA8a consists of a 15 m thick succession of interbedded greenish, laminated, carbonaceous shales (Fh) with lignite streaks, and siltstones (Slm). FA8b comprises a 70 m thick, fining-upward succession of sub-tabular geometry and complex lateral facies relationships, composed from the base upward of massive, pebbly sandstone (Sm) with abundant shelly layers followed by massive, well-stratified, upper-medium-grained sandstones (Sm) grading to lower-medium-grained, tangential trough cross-bedded (~50 cm height) sandstones (St) with reactivation surfaces and capped by bidirectional-cross stratified beds (Shb) (Fig. 4g) showing mud partings and tidal bundles (Fig. 4h) often intercalated with horizontal-planar laminated sandstones (Spl). The succession continues with fine- to very fine-grained sandstone showing trough cross-stratification (St; ~1 m wavelength and < 0.15 m high; Fig. A1i) and planar lamination (Spl) grading laterally to medium-grained, cross-bedded sandstones (Spa, St, Shb) with scour-and-fill structures, mud drapes

and tidal rhythmite (Hlh) intercalations. FA8c consists of a 60 m thick, laterally continuous (km scale) coarsening- to thickening-upward succession comprised by interbedded mudstones/siltstones and very fine-grained sandstones (Hlh) with well-developed horizontal-planar lamination, in some cases with a low angle inclination (< 5° dipping southward; Fig. 4i, j). These are commonly interrupted by scoured, lenticular to sub-tabular, medium- to fine-grained, massive, coarsening-upward, shelly sandstones and conglomerates (Sm, Gs) (Fig. 4i) with upper plane laminated tops (Spl), or by fine- to very fine-grained sandstone beds with herringbone cross-lamination (Shb) (Fig. 4g), as well as epsilon or tangential-based, trough cross-lamination with mud drapes (St). A 15 m thick, crudely fining-upward (medium- to fine-grained) tabular sandstone divides the succession into two segments (Fig. 3b) and is characterised by well-stratified, massive to low-angle planar cross-laminated sandstones (Sm, Spl) with diffuse ripple cross-lamination (Sr) and numerous conglomeratic shelly lenses (Gs). The BI is variable according to each sub-facies association, but in general, the trace fossils are of small size (compared to the previous FAs). FA8b has low bioturbation (BI 0-1), where some *Skolithos* isp. (Fig. A1.9) are observed. FA8c has high bioturbation (BI 4-5), restricted to the heterolithic facies, where pervasive bioturbation precludes identification of single trace fossils. However, in some indistinct mottled and crumbly textures, vague *Planolites* isp. and *Palaeophycus* isp. are present. Palaeocurrents directions vary according to each FA, but in general, yield a southward trend with modes to the northwest, east, and west.

We interpret FA2, 3 and 4 to represent an offshore transition, lower to middle shoreface, and middle to upper shoreface (and foreshore), respectively. The amalgamation of hummocky cross-stratified-rich beds and the transition from hummock- to swaley-dominated units in FA4 suggest multiple episodes of erosion triggered by intense storms in areas close to the shoreline (Malkowski et al., 2016). The abundance of organic detritus in FA4 likely denotes fluvial influence or the proximity to plant-rich areas. On the other hand, the dominance of Fh and Fm facies along with open-marine ichnofossils in FA5 suggest a low-energy offshore marine setting, below storm-wave base. The

intercalations with Slm, Sm, and Shcs reflect periods of wave-induced reworking during storm events and/or rapid fallout of sands triggered by hyperpycnal density underflows (Bhattacharya, 2010; Rossi and Steel, 2016). Its relationship with FA6 suggests that FA5 was deposited in a prodelta environment.

The cross-bedded and massive sandstones (St, Sm) in FA6a likely represent deposition under rapidly decelerating unidirectional flows in sandy delta fronts (Bhattacharya, 2010). A fluvial influence is expressed by the abundance of carbonaceous fragments, scours and pebbles, and locally stressed conditions (Schwartz and Graham, 2015). However, the presence of Slm, Spl and Shcs facies suggests shallow-wave reworking processes of these distal delta front deposits. Coarse sandstones overlying scoured surfaces in FA6c indicate bedload deposition by fluvial currents and, considering their association with planar- and trough cross-stratified (subaqueous 2D/3D dunes) beds, we interpreted them as terminal distributary channels (Olariu and Bhattacharya, 2006). Dune-scale trough cross-bedding (FA6b) suggests high-energy currents able to develop 3D dunes migrating seaward. Such a high-energy regime is supported by the paucity of bioturbation and various scour-and-fill structures, which in turn suggest the landward connection of these subaqueous dunes with terminal distributary channels (FA6c). FA6b can be interpreted as short clinoform sets developed in a distal mouth bar, possibly indicating the rollover point of the delta front (Bhattacharya, 2010; Le Roux et al., 2010; Schwartz and Graham, 2015). In general terms, we interpret FA6 to represent a wave-influenced (if not dominated) delta front environment.

In sections CP and SD, the fining-upward succession arranged from the base up by Spa, St, Sr, Spl, and Slh facies represent point-bar deposits of meandering rivers (Miall, 2014), although the presence of carbonaceous material, shell lags, and wavy tops on channels suggest occasional wave reworking. Overbank deposits are represented by units with Sw, Slh, and Sr facies, where organic matter, wood fragments, and pedogenetic nodules are present. The coarse-grained, sediment-rich units represent bed-load deposits of braided rivers with channel-lag and gravel sheets or bars (Gmm,

Gmg) and planar to cross-stratification (St, Spl) traction structures indicate lower- to upper-flow regime (Miall, 2014). The sub-angular sandstone and mudstones clasts represent channel lag intraformational conglomerates. In contrast, the sub-rounded basaltic, andesitic, and chert pebbles suggest an extrabasinal input of a nearby fold-thrust belt. We interpret FA7 to represent fluvial deposits.

Finally, the relatively thick (>70 m) sandstone-dominated succession of FA8a which present Sm, St, Spl, shell-rich and pebbly layers with *Skolithos* isp. suggest deposition under moderate- to high-energy conditions in a nearshore environment. This is interpreted as representing a barrier spit or submerged bar (Dalrymple et al., 1992; Reinson, 1992; Plink-Björklund, 2008; Le Roux et al., 2010). The overlying (0-16 m interval, see Fig. 3b) medium-scale, tangential, trough cross-bedded sandstones (St) associated with Shb and Hlh facies, and abundant reactivation surfaces, scour-and-fill structures, and mud drapes reflect the existence of reversing currents (e.g., ebb and flood flows) of variable strength and strongly affected by tidal ravinement; their association with barrier deposits suggests that these are tidal-inlet deposits (Dalrymple et al., 1992; Reinson, 1992; Plink-Björklund, 2008). We interpret the overall FA8a as a high-energy estuary mouth complex. In FA8b, the heterolithic units (Hlh) are interpreted as sandy tidal mudflats (*sensu* Flemming, 2000) near to river mouths where alternation of tractional sand deposition and mud fallout during slack water periods prevailed, while the large-scale, low-angle inclined heterolithic beds can be associated with laterally accreted point bars of meandering tidal channels (Thomas et al., 1987). The horizontal-planar lamination on the tops of the sandstones and shell-rich conglomerates that are intercalated within the sandy tidal mudflats, and the Spl facies may indicate wave action on local submerged sandy and/or shell-rich bars, or local beaches developed along the edge of the tidal flats, respectively (Le Roux et al., 2010). The fining-upward sandstones with Shb, and St facies and paired mud drapes are interpreted as point bar deposits of tidal creeks. On the other hand, the thick, tabular, fining-upward, sandstone bed dividing the succession is interpreted as distal distributary mouth bars affected by

dense underflows and/or seasonal river discharges transporting brackish water fauna (Plink-Björklund, 2008; Le Roux et al., 2010). The latter is supported by laterally coarsening-upward and inversely graded shelly sandstones and conglomerates. The association of Fh and Slm facies with coal streaks suggests deposition by suspension during low-energy conditions but frequently punctuated by clastic influx in a marsh plain surrounding the landward side of a lagoon or tidal flat. Overall, FA8b represents a middle to inner estuary sub-environment.

4.1.4 Chorrillo Chico Formation

FA9 dominates the Chorrillo Chico Formation in sections RB, PP, PC (Table 1, Fig. 2d) and overlies FA4 of the Rocallosa Formation. In section RB, this formation consists of a coarsening- and thickening-upward succession of mudstones (Fm), massive to normally graded glauconitic siltstones (Slm) and very fine- to medium-grained sandstones (Sm). FA9 is characterised by sharp-based Slm and Sm facies that comprise individual units 10-90 cm thick, interbedded with thick Fm or Slm facies. Amalgamated beds (0.9 m to 1.2 m thick) consist of (from the base upward): medium-grained, massive sandstones (Sm) with slightly erosive to planar bases, overlain by fine-grained, wispy, planar- or ripple-laminated sandstones (Sw, Spl, Sr) grading upward to convolute layers (Fig. 4k) or Slm/Fm intercalations capped by Fm facies. In section PP, the basal part of the formation includes Fm facies intercalated with bioturbated (clean or glauconitic) sandstones with loaded bases and flames. Angular flakes of coaly wood fragments (aligned preferentially NNW; Fig. A1j) and angular to sub-angular glauconite and pumice pebbles fill scours. Contorted bedding in mudstones and sandstones (Fig. 4l), and flutes are common. Bioturbation is intense (BI 3-6) and characterised by ichnogenera such as *Thalassinoides* isp., *Neonereites* isp. (Fig. A1.10), *Scolicia* (*Laminites*) (Fig. A1.11), *Asterosoma* isp., *Zoophycos* isp., *Phycosiphon incertum*, *Planolites* isp., *Chondrites* isp., *Ophiomorpha nodosa*, *Rhizocorallium* isp. (Fig. A1.12), *Paradictyodora*?, *Taenidium barreti*, *Nereites missourensis*, and local occurrences of *Skolithos* isp. Palaeocurrent indicators yield palaeoflow to the NW. Similarly, palaeocurrents in the Cabo Nariz beds are towards the northwest.

Individual beds are interpreted as a low-density turbidity currents deposits because the basal tool marks, traction structures and normal grading indicate layer-by-layer deposition under turbulent and subsequent waning flow conditions (Shultz et al., 2005; Haughton et al., 2009; Romans et al., 2009; Malkowski et al., 2017a). Massive sandstone beds (Ta), wispy, planar- or ripple-laminated sandstones (Tb, Tc), as well as interbedded siltstones and mudstones (Td) capped by mudstones beds (Te) correspond to internal Bouma divisions (Fig. 4l). However, the presence of angular, coaly wood fragments, glauconite, and pumice pebbles (Fig. A1k) within a fine-grained matrix filling scours is interpreted as debris-flow deposits (H3) and together with the alternating bioturbated (clean or glauconitic) sandstones (H2, H1) within mudstones could represent internal sub-divisions of hybrid beds (Haughton et al., 2009) linked to turbiditic deposits. The trace fossil assemblage shares characteristics of the *Zoophycos* and *Nereites* ichnofacies (Buatois and Mángano, 2011) and given the benthic foraminifer content (Charrier and Lahsen, 1969; Rivera, 2017), both suggest deposition in bathyal water depths. Similar facies have been recognised in deep-water turbidites elsewhere in the basin where it is associated with relatively distal or off-axis deposition in lower fan, basin plain or slope settings (Shultz et al., 2005; Romans et al., 2009; Malkowski et al., 2017a).

4.2 SANDSTONE PETROGRAPHY AND DETRITAL ZIRCON GEOCHRONOLOGY

4.2.1 Modal composition and detrital zircon U-Pb age distribution

Rocallosa and Dorotea formations. Sandstones are classified as lithic arkose. Monocrystalline quartz constitutes 82% of the total quartz grains in the samples, whereas the feldspar grains are almost in the same proportions between plagioclase (59%) and potassium feldspar (41%). Potassium feldspar (commonly altered; Fig. 5a) is dominated by microcline and orthoclase with perthitic textures (Fig. 5b). The lithic fragments are mainly volcanic (60%; Fig. 5a), followed by metamorphic (21%; Fig. 5c, d), and sedimentary rocks (19%; Fig. 5e). Some well-preserved plutonic fragments are also observed (Fig. 5f). Volcanic lithics are dominated by felsitic (44%; Fig. 5f, g) and microlitic textures (36%; Fig. 5h), whereas the metamorphic lithics are mainly micaceous schist (Fig.

5c), and (meta-) volcanics (Fig. 6g). There are also pelitic fragments (Fig. 5e) accompanied by tremolite-actinolite and chlorite minerals. The detrital zircon age spectrum in sample ZPR1 ranges from 67.7 to 276.5 Ma and shows three significant age peaks at 68-81 Ma, 93-107 Ma, and between 142-160 Ma, with a small peak at 277 Ma (Fig. 6a). The detrital zircon age distribution of sample ZLP1 is similar to that of ZPR1, ranging from 67.1 to 2204 Ma, with main peaks at 69-73 Ma, 92-108 Ma, and 146-171 Ma, but older zircon peaks at 272-315 Ma, 615-640 Ma, and 1930-2200 Ma are better represented (Fig. 6a).

Chorrillo Chico Formation. The sandstones are classified as lithic arkose. Monocrystalline quartz (91%) dominates and increases up-section. Plagioclase (64%) is the main feldspar, but samples closer to the Rocallosa contact are potassium-feldspar-rich and impoverished in lithic fragments. The dominant lithic fragments are of volcanic origin (62%), followed by sedimentary lithics (29%; Fig. 5e) and, to a lesser extent, metamorphic lithics (metapelites; 9%). Volcanic lithics show mainly microlitic (47%; Fig. 5h), lathwork (29%; Fig. 5i), and felsitic textures (12%), but some devitrified volcanic lithics (Fig. 5j) and plutonic fragments (Fig. 5f) are also observed. In general, the sedimentary lithic content increases up-section, as do the abundance of chert and vitric shards (Fig. 5k). The glauconite grains are fragmented and reworked unlike those of the Rocallosa Formation, which are mainly authigenic. The detrital zircon age distribution of sample PB1 ranges from 54 to 131 Ma and contains a dominant age peak at 65-100 Ma (Fig. 6a). A minor subpopulation that is not discriminated on the probability density curve but differentiated in the raw data ranges from 54-60 Ma (Paleogene), and 110-131 Ma (early Cretaceous). In this sample, the absence of late Jurassic and much older grains is apparent. For sample RB1, detrital zircon U-Pb ages range from 64 to 655 Ma and are characterised by three significant age peaks at 67, 77, and 95 Ma and a small peak at 108-113 Ma (Fig. 6a). Additionally, a few older grains of early Cretaceous (134 Ma; 1 grain), and Paleozoic-Neoproterozoic (528-655 Ma; 2 grains) ages are present.

Cabo Naríz beds. The sandstones are classified as feldspathic litharenite. Monocrystalline quartz (80%) dominates in all the studied samples, whereas potassium feldspar (60%) slightly outweighs the plagioclase (40%) content. The lithic fragments are mainly volcanic (74%), followed by metamorphic (17%), and sedimentary rocks (8%; which increase up-section). Lathwork (56%) and felsitic (35%) textures predominate in volcanic lithics (Fig. 5g, i), and micaceous schists in the metamorphic fragments (Fig. 5c). Notably, lower samples from the Cabo Naríz beds are enriched in potassium feldspar, monocrystalline quartz, as well as metamorphic and felsitic volcanic lithic fragments. The detrital zircon age distribution of the Cabo Naríz samples (Sánchez et al., 2010) shows a dominant age peak at 75 Ma, and other significant peaks at 58, 88-94, and 107 Ma, with some minor age peaks at 131 and 161 Ma, and a few Paleozoic-Mesoproterozoic grains also present (Fig. 6a).

4.2.2 Provenance record inferred by U-Pb ages and compositional data

The mean modal composition of the Rocallosa-Dorotea Formations ($Q_{34}F_{44}L_{22}$, $Qm_{25}F_{44}Lt_{30}$) and Chorrillo Chico Formation ($Q_{34}F_{44}L_{22}$, $Qm_{27}F_{44}Lt_{30}$) reflects a dissected arc tectonic field (Dickinson, 1985) (Fig. 7), which suggests that those units were derived from the unroofing of the Andean magmatic arc (including plutonic roots and volcanogenic material). A similar interpretation applies for the Cabo Naríz beds ($Q_{19}F_{31}L_{50}$, $Qm_{31}F_{44}Lt_{54}$; misinterpreted as the Cerro Toro Formation in Romans et al. 2010), in which samples plot within the transitional arc field (Dickinson, 1985). Some subtle compositional trends are observed in the Chorrillo Chico Formation (Fig. 7) of which the modal signature of the basal samples is more related to the basement uplift field and for the uppermost samples to the recycled orogen field (Dickinson, 1985). For the Cabo Naríz beds, a compositional trend is unclear despite the richness in K-feldspar and monocrystalline quartz of the lower samples. The Rocallosa-Dorotea formations samples also lack a clear trend.

Based on the presence of Campanian to Paleocene (~80-56 Ma) detrital zircon ages both in the Dorotea-Rocallosa and Chorrillo Chico-Cabo Naríz samples, coincident with the assigned

biostratigraphic ages for those formations (Fig. 6a), we interpret a continuous delivery of arc material from the Southern Patagonian Batholith (Hervé et al., 2007). The presence of plutonic fragments and K-feldspar with perthitic exsolution (Fig. 5b, f) in the Rocallosa-Dorotea and Chorrillo Chico formations supports the exhumation of arc roots. The overall abundance of microlitic textures (Fig. 5h) and the relatively high proportion of plagioclase in the studied samples indicate erosion of an andesitic to mafic volcanic carapace in the Andean magmatic arc system. Moreover, microlitic textures with palagonite filling vesicles present in the Rocallosa-Dorotea samples could indicate the input of basaltic lava fragments from the mafic Barros Arana-La Pera complexes (Stern et al., 1991). On the other hand, the abundance of Campanian to Hauterivian (~130-80 Ma.; Fig. 6a) detrital zircon ages suggests either continued input of Cretaceous plutons of the Southern Patagonian Batholith or erosion of Cretaceous foreland deposits hosting significant arc-derived zircons. We cannot rule out the latter possibility given the presence of sedimentary lithics (Fig. 5e) in the samples.

Middle Jurassic to early Cretaceous detrital zircon ages (~170-135 Ma.; Fig. 6a), mainly in the Rocallosa-Dorotea and (lower) Cabo Naríz samples, indicate that RVB remnants and the Tobífera Formation contributed detritus to the basin. Volcanic lithics with lathwork textures (Fig. 5i) present in all the studied samples corroborate the input of basaltic lava fragments from the ophiolitic suites of the RVB, whereas the felsitic, and devitrified textures (Fig. 5j, g) support the exhumation of the volcaniclastic Tobífera Formation. On the other hand, Palaeozoic to Paleoproterozoic detrital zircon ages (~270-2200 Ma; Fig. 6a) associated with micaceous schists and other metamorphic fragments (Fig. 5c, d, g) in all samples, suggest the incorporation of metamorphic (Andean and Cordillera Darwin Metamorphic complexes) source terranes in the hinterland to the west (Fig. 1a), which is consistent with the heavy mineral suite identified by Charrier and Lahsen (1969). However, we cannot rule out the probable contribution of Palaeozoic zircons from the Río Chico-Dungeness Arch (Fig. 1a) in the Dorotea strata, as previously suggested by Gutiérrez et al. (2017) 100 km north of our study area.

The relative contribution from the Tobífera Formation and coeval Jurassic intrusives (Pankhurst et al., 2000; Calderón et al., 2007; Hervé et al., 2007) together with reworked grains of the Andean Metamorphic Complexes (Hervé et al., 2003, 2010; Barbeau et al., 2009) appear to have been more significant during deposition of the Rocallosa-Dorotea formations (latest Campanian to late Maastrichtian) compared to the Chorrillo Chico Formation (Paleocene) (Fig. 6c). Furthermore, this provenance shift can be distinguished to the north of our study area (at Sierra Baguales), and in the Chilean part of Tierra del Fuego (Fig. 6c), most likely suggesting a regional change in the sediment distribution system.

Components of the Tobífera Formation and metamorphic basement, relatively more abundant in the lower members of both the Chorrillo Chico Formation and the Cabo Naríz beds, decreases up-section. At the same time, microlitic volcanic lithics and vitric shard fragments increase up-section, suggesting intermediate to felsic synsedimentary volcanism. This Paleocene volcanic event is recorded in the whole basin (Charrier and Lahsen, 1969; Macellari et al., 1989; Torres-Carbonell and Olivero, 2019).

4.2.3 Maximum depositional ages

From the provenance data, it is apparent that the Southern Patagonian Batholith maintained protracted connectivity with the foredeep, providing syndepositionally formed zircons. This connectivity allows estimates of reliable maximum depositional ages very close to the true depositional ages. Sample ZPR1 has a youngest single grain of 67.7±2.4 Ma and a calculated maximum depositional age of 73.5±1.3 Ma from n=2 grains (Fig. 6b). Sample ZLP1 has a youngest single grain of 67.1±1.6 Ma and an estimated maximum depositional age of 67.7±1.2 Ma from n=3 grains (Fig. 6b). Sample RB1 has a youngest single grain of 64.4±1.3 Ma and a calculated maximum depositional age of 64.7±0.67 Ma from n=4 grains (Fig. 6b). Sample PB1 has a youngest single grain of 59.2±3.1 Ma and a calculated MDA of 60.7±2.2 Ma from n=3 grains (Fig. 6b).

4.3 PALYNOLOGY

From the three samples analysed in the Rocallosa Formation (Fig. 2c, 3a), the palynomorph content (Table 3) displays a terrestrial predominance over dinocysts, which are commonly poorly preserved but can tentatively be identified as *Spiniferites* sp. In order of abundance, epiphytic fungi (40.9%), including *Granatisporites* sp. (Fig. 8a), *Multicellaesporites* sp. (Fig. 8b), and *Monoporisporites* sp.; magnoliophytes (27.7%), including *Nothofagidites brassi* type (Fig. 8c), *N. dorotensis* (Fig. 8d), *N. cincta* (Fig. 8e), *N. diminuta, N. flemingii, N. spinosus, Gaultheria* sp., *Tricolpites* sp., and *Monocoplites* sp.; pteridophytes (21.4%), including *Laevigatosporites vulgaris* (Fig. 8f), *Cyathidites minor, Gleicheniidites senonicus, Clavifera triplex* (Fig. 8g), *Lycopodium austroclavidites, Polypodiisporites* sp., *Gleicheniidites* sp.; Pinophytes (7%), including *Podocarpidites otagoensis* (Fig. 8h), *P. marwickii,* and *Araucariacites australis;* microalgae colonies (3%), represented by *Botryococcus braunii* (Fig. 8i), are present.

The dominance of terrestrially-derived palynomorphs suggests proximity to the area of continental supply. The association of epiphytic fungi spores, *B. braunii* (Fig. 8i), dinocysts, and pteridophytes (Fig. 8f, g) suggests a marginal estuarine/deltaic brackish environment with a considerable influence of freshwater. It also reflects a highly alkaline and generally oligotrophic environment surrounded by poorly drained areas, probably developing local peat swamps on the damp rainforest floors, where an understorey of shade-tolerant ferns could flourish (Palma-Heldt, 1983; Borel, 2007; Bowman et al., 2014). The association of *Podocarpidites, Nothofagidites*, and pteridophytes suggests that these dense forests flourished in low coastal areas and humid environments. Typically, *Araucariacites* and *Podocarpidites* thrive in elevated areas; however, they have proven to be adaptable and can also be linked to relatively low areas related to coastal and/or marsh environments (Quattrocchio et al., 2006). On the other hand, *Araucariacites* and *Podocarpidites* characterise the temperate-cold rainforest of the austral regions (Palma-Heldt, 1983). In contrast, Cyatheaceae currently develops in pantropical regions, and their abundance would also indicate hot and humid palaeoclimatic conditions (Povilauskas, 2017). However, they are more

sensitive to variations in humidity than to temperature (Palma-Heldt, 1983). *Nothofagidites* is the essential genus that inhabits the sub-Antarctic forests of Patagonia and is associated with areas of high humidity (Palma-Heldt, 1983; Herngreen et al., 1996) and temperate climate (Carrillo-Berumen et al., 2013). Particularly the *N. brassii* type (Fig. 8c) is related to temperate-warm climates and low-elevated areas. In synthesis, the palynofloristic association and its relative percentage of abundance allow us to interpret a cool-temperate (6-12°C) to warm-temperate (12-17°C) climate with humid and rainy conditions for the Maastrichtian-Danian.

5. DISCUSSION

5.1 Evolution of depositional systems

The transition of deep-marine to shallow-marine deposits recorded by the Fuentes and Rocallosa formations (Fig. 3a) in the Magallanes Province, and by the Tres Pasos and Dorotea formations (Fig. 3b) in the Ultima Esperanza Province, signals an upward-shoaling cycle. This cycle 1 began as early as the Cenomanian in the northernmost part of the basin near Lago Argentino (Malkowski et al., 2017b), by the late Campanian to early Maastrichtian in our study area, and as late as the late Paleocene in the southernmost part of the basin in Tierra del Fuego (Olivero et al., 2003; Martinioni et al., 2013; Torres Carbonell and Olivero, 2019) (Fig. 2a). In the Magallanes Province, the uppermost Fuentes Formation is characterised by outer shelf to upper slope environments that grade rapidly to an offshore-transition environment (Figs. 3a, 9a), where sedimentation was related to turbidity currents. Cycle 1 continued with the establishment of shoreface environments of the Rocallosa Formation (Figs. 3a, 9a), where waves and storms were the main sediment transport mechanisms. Palaeocurrents and provenance data suggest sediment dispersal from the fold-thrust belt in the northwest to the west (Fig. 9c). In the Ultima Esperanza Province, the shift from slope deposits of the Tres Pasos Formation to a deltaic system of the Dorotea Formation (Shultz et al., 2005; Romans et al., 2009; Schwartz and Graham, 2015; Gutiérrez et al., 2017) (Fig. 9a) represents this cycle 1. Palaeocurrent directions of the Dorotea Formation indicate progradation towards the south

(Fig. 9c), although the provenance data (Fig. 6a) suggest sediment input from the west. The lower and middle part of the Dorotea Formation (in section SD; 51°40'S) represents a wave-dominated deltaic depositional system (Figs. 3b, 9a), which hindered the clear distinction between shoreface and delta front and inhibited the development of a large number of terminal distributary channels (cf., Olariu and Bhattacharya, 2006; Bhattacharya, 2010). Farther south, in section CP (52°S), the Dorotea Formation represents a storm-dominated shoreface depositional setting. The uppermost Dorotea Formation exhibits both fluvial deposits of different types (meandering in section SD and braided to meandering in section CP), as well as estuarine deposits. The significantly large dimensions of the shoreface-incised (fluvial) channels (in section CP) along with the overlying succession of estuary deposits, lead us to interpret them as incised valley fills.

An incised valley interpretation for the shoreface-incised channels of section CP is supported by the (1) multi-storey channels that record an abrupt basinward facies shift (Fig. 3b); (2) the bounding erosion surface at the base of incised channels correlating with angular unconformities to the north of the basin (at the base of the Calafate Formation) (Fig. 10a); and (3) the estuarine infill onlapping the valley walls in a landward direction (Fig. A1g). These features meet the recognition criteria for incised valleys, as outlined by Zaitlin et al. (1994). The internal vertical evolution of the incised valley fill is reflected by the transition from braided fluvial channels to a meandering fluvial system followed by a protected estuary environment affected by tides (Figs. 3b, 9b), which imply a mixed energy scenario for the incised valley system. Member D of the Rocallosa Formation (*sensu* Charrier and Lahsen, 1969) in the Magallanes Province, could be the equivalent to the fluvial deposits at the base of the incised valley systems identified in Ultima Esperanza Province as it reflects a change to higher-energy conditions, suggesting the establishment of a Gilbert-type delta in a landward (westerly) position (Fig. 9b). Gilbert-type deltas are dominated by stacked mass flows (boulders and cobbles) and fluvial traction sedimentation (frequently reworked by waves) in their topsets, while foresets and bottomsets are dominated by subaqueous sediment-gravity flows of coarse

to very coarse sand, slumps, and down-slope turbidity currents (Falk and Dorsey, 1998; Rojas and Le Roux, 2005). The facies presented in the stratigraphic column of La Pesca Bay (Fig. 3a) could be interpreted as the topset-foreset transition, dominated by slumps, high-density turbidity current deposits or sediment gravity flows (Lowe, 1982).

The estuary environment in Ultima Esperanza Province and the deep-marine facies of the Chorrillo Chico Formation and Cabo Naríz beds in Magallanes Province and Chilean Tierra del Fuego (Fig. 9b) represent the change to cycle 2. This cycle 2 is characterised by deepening of the environments within the basin and represents the sedimentological record of the Maastrichtian-Danian transgression. Cycle 2 is apparent in the northernmost Lago Argentino area (Fig. 2a), where it is depicted by the transition from Campanian to early Maastrichtian non-marine deposits to estuary systems developed in incised valleys (Marenssi et al., 2004) or shoreface to offshore-transition deposits (Odino et al., 2018) of the Calafate Formation. In the Chorrillo Chico Formation, dilute turbidity currents with episodes of sediment gravity flows were critical components of the middle and distal turbidite fan system. Turbidite currents develop most likely by both erosion of the shoreface, as suggested by the highly fragmented and reworked glauconite grains, and by slope disequilibrium (e.g., Haughton et al., 2009). Such processes could be influenced by tectonic deformation in the nearby fold-thrust belt, as has been previously suggested for time-equivalent strata in Tierra del Fuego (Sánchez et al., 2010; Martinioni et al., 2013; Torres Carbonell and Olivero, 2019). Palaeocurrent directions towards the northwest in the Cabo Nariz beds and Chorrillo Chico Formation (Fig. 9c) suggest a connection between both turbidite deposits. Thus, the observed coarsening- and thickening-upward trend in both formations (Sánchez et al., 2010) depicts a northwest-ward prograding submarine fan system aligned with the foredeep axis, with the channelised upper fan in Tierra del Fuego and the outer fan to fan-fringe in the Brunswick Peninsula.

5.2 Sequence stratigraphic architecture

Sequence 1. The basal sequence boundary (late Campanian, ~73.5 Ma) is well represented in the northernmost part of the basin (Lago Argentino) by the late Campanian disconformity that separates the La Anita and La Irene formations (Macellari et al., 1989). In our study area, such disconformity is not apparent. However, Mpodozis (in Álvarez et al., 2006) notes a disconformity between the Tres Pasos and Monte Chico-Dorotea formations, ~50 km to the north of our study area, in the Cerro Cazador area (Fig. 2a). The limit between the Tres Pasos-Dorotea formations at Cerro Cazador is approximately late Campanian in age (~73.5 Ma; Daniels et al., 2019). In our study area, the lowstand (LST) and transgressive (TST) systems tracts correspond to segments of the Tres Pasos Formation not studied here. Only the overlying highstand system tract (HST) can be recognised (Fig. 10a), manifested in the Ultima Esperanza Province by the transition from shelf deposits of the Tres Pasos Formation (Gutiérrez et al., 2017) to deltaic deposits of the Dorotea Formation (Fig. 10b). Internally in the Dorotea Formation, the vertically-stacked parasequences (clinothems) passing from prodelta to mid-to-upper shoreface (Fig. 3b) suggest a progressive aggradational to progradational stacking pattern (denoting landward changes in the shoreline trajectory; Fig. 10b) and reduction of basin accommodation. In the Magallanes Province, the HST is represented by the prograding shoreface deposits of the Rocallosa Formation overlying the aggrading outer shelf to upper slope environments (Fig. 10c) of the uppermost Fuentes Formation. This transition might represent the maximum flooding surface (MFS) giving rise to the beginning of a normal regression (Fig. 10c), where sedimentation tended to balance or outpace the rates of base-level rise.

Sequence 2. The sequence boundary (late Maastrichtian, ~68.9 Ma) is an angular unconformity that separates the Chorrillo Formation of the late Maastrichtian Calafate Formation in the northernmost part of the basin (Lago Argentino area) (Macellari et al., 1989; Marenssi et al., 2004). This angular unconformity correlates with the regional incision surface at the base of the incised valleys in the Ultima Esperanza Province (Fig. 10a), whose early deposits yield a maximum depositional age of 67.7±1.2 Ma (late Maastrichtian). This unconformity is manifested in the

Magallanes Province as correlative conformity (Fig. 10a, b). The incised valleys were composed of a low-sinuosity fluvial system which was interpreted as low-accommodation lowstand fluvial deposits (Fig. 3b). At the same time, in the Magallanes Province, the LST is represented by the Gilbert-type delta in Member D of the Rocallosa Formation (Fig. 3a). The vertical change from a braided to high-sinuosity fluvial style with well-developed floodplains (in section CP; Fig. 3b) indicates an increase in basin accommodation; followed by a progressive marine influence on the low-amalgamated, fluvial channels (in section SD; Fig. 3b); which are abruptly overlain by lagoon and mire deposits. The increased accommodation is also reflected by the basal mudstone-dominated interval of the turbidite succession at the base of Chorrillo Chico Formation as observed in the Magallanes Province (Fig. 10c). In the Lago Argentino area, the shift from fluvial (Chorrillo Formation) to nearshore or shoreface deposits of the Calafate Formation (Marenssi et al., 2004; Odino et al., 2018) attests to the increase in accommodation. The long-term evolution from fully fluvial systems to an estuary or shoreface in the north of the basin, and upper shoreface deposits to deep marine deposits in the south, suggests a backstepping stacking pattern representing a TST (Fig. 10b, c). The development of floodplain deposits indicates the commencement of the TST (section CP; Fig. 3b) whereas the wave-ravinement scouring represents the transgressive surface (TS) (Fig. 4e) of the fluvial channels (in sections SD and CP) in the Ultima Esperanza Province. The location of such a surface in the Magallanes Province is less precise, but it is assumed to be represented by the boundary between the Rocallosa and Chorrillo Chico formations (Fig. 10c). We infer that the development of distal distributary mouth bars (section SD) in the inner to middle estuary sub-environment of the uppermost Dorotea Formation (Fig. 3b), might evidence the onset of an early stage of regression. Therefore, we place an MFS at the base of the distal distributary mouth bars (Fig. 10b) and in the transition to a sandstone-dominated turbidite system of the Chorrillo Chico Formation (Fig. 10c) that indicates the commencement of an HST. The uppermost sequence boundary is represented by the ~18 Myr unconformity between the Dorotea (Maastrichtian-Danian) and Rio Turbio (Eocene) formations in

the Ultima Esperanza Province (e.g., Malumián and Caramés, 1997; Gutiérrez et al., 2017; George et al., 2020). Farther south, in the Magallanes Province, the uppermost sequence boundary is represented by the ~3 Myr gap between the Chorrillo Chico and Agua Fresca formations (Rivera, 2017), manifested in outcrops as correlative conformity. It is important to mention the diachroneity of this sequence boundary, marked at ~61 Ma in the Ultima Esperanza Province and by ~58 Ma in the Magallanes Province.

The southward diachroneity of unconformities or sequence boundaries and the recurrence of correlative conformities-bounded sequences are noteworthy (Fig. 10a). These features seem to be coincident with the southward increase in lithospheric attenuation during the precedent extensional phase of the RVB (Malkowski et al., 2016), highlighting a probable interdependency.

5.3 Forcing signals on the Maastrichtian-Danian transgression

5.3.1 Role of climate

Patagonian transgressions are typically linked to warm climatic episodes and are generally associated with abundant large size forams or thermophilic biota (Malumián and Náñez, 2011). However, the Maastrichtian-Danian transgressive deposits lack such faunal assemblages (Malumián and Náñez, 2011) and $\delta^{18}O$ isotopes records in the South Atlantic suggest cold water temperatures during the late Santonian and until the Danian (Barrera and Savin, 1999; Cramer et al., 2009; Le Roux, 2012) (Fig. 1b). Similarly, high-resolution palynological studies in the Antarctic Peninsula (Bowman et al., 2014) indicate a cooling trend between the early Maastrichtian to Paleocene. In the MAB, stable oxygen isotope records at the base of the Chorrillo Chico Formation (*ca*. 65.2 Ma) suggest a cool palaeoclimate (Sial et al., 2001). This generalised cooling trend rules out any link of the Maastrichtian-Danian transgression with warm climatic events.

While oxygen isotope records favour cold climatic conditions during the Maastrichtian to early Paleocene, our palynological results (Table 3) suggest more temperate conditions (~6-17°C) in

the MAB. We envisage a dynamic climatic system with fluctuations between cool and warm conditions. The latter supports the hypothesis of del Río et al. (2015) that the MAB could be placed in a transitional area between warmer and cooler temperate waters of northern Patagonia and the Antarctica Peninsula, respectively. Our paleoclimatic reconstruction also suggests humid and rainy conditions during the Maastrichtian-Danian. These humid and rainy conditions also prevailed in the Antarctic Peninsula at this time (Bowman et al., 2014).

5.3.2 Tectonic versus eustatic triggers

Previous research dealing with sea-level changes or the Maastrichtian-Danian transgression in Patagonia invokes eustatic forcing as the causative mechanism of base-level changes (e.g., Malumián and Nañez, 2011; Vallekoop et al., 2017). However, the progressive decrease of the long-term eustatic sea-level from the late Campanian (Fig. 1b) suggests that eustasy was not the controlling mechanism for the Atlantic transgression in Patagonia. Local or regional tectonism is an alternative, more likely explanation for the origin of the marine ingression, although only a few studies in the region suggested this mechanism (e.g., Aguirre-Urreta et al., 2011; Gianni et al., 2018).

The late Maastrichtian basal unconformity in sequence 2 (Fig. 10), represented by the erosion surface at the base of the incised valley systems of the upper Dorotea Formation in the Ultima Esperanza Province, and by the angular unconformity at the base of the Calafate Formation in the Lago Argentino area (Macellari et al., 1989) suggests tectonic activity across the MAB by the end of the Cretaceous. The sandy gravel and coarser deposits, typically sub-rounded or sub-angular, in the early fill of the incised valley systems, as well as the abrupt shift to a high-energy Gilbert-type delta setting in member D of the Rocallosa Formation in the Magallanes Province, suggest rivers draining a tectonically active region (Li et al., 2006; Torres Carbonell and Olivero, 2019). Moreover, the turn-over of basement-derived sediments to chert and sedimentary lithics in the Chorrillo Chico Formation and Cabo Nariz beds, as well as their orogen-recycled signature trend (Fig. 7) reflect thrust belt advance during the early Paleocene. This thrust belt activity inferred by the sedimentary

record is consistent with the results of structural studies that suggest active deformation and the advancement of the orogenic wedge in both the Ultima Esperanza Province and Tierra del Fuego during the Maastrichtian-Danian (Fosdick et al., 2011; Torres-Carbonell et al., 2013).

Deformation in the orogen generated increased loading, which in turn, caused increased flexural subsidence during the Maastrichtian-Danian. The change from shoreface environments to deep-water sedimentation in the Chorrillo Chico Formation, as well as the development of estuarine environments during the late filling stages of the incised valleys in the uppermost Dorotea Formation, reflect an increased accommodation as a result of enhanced basin subsidence. Biddle et al. (1986) and Mpodozis et al. (2011) described the wedge geometry of Maastrichtian-Paleocene deposits across the MAB, which thicken westwards, preserving the asymmetric geometry of a subsiding foreland basin. Furthermore, Biddle et al. (1986) and Mella and Sánchez (2000) based on 1D well backstripping showed that the foredeep recorded accelerated subsidence between the Maastrichtian and Paleocene (Fig. 11).

Although our study stresses active regional tectonism in the orogenic wedge as the trigger of subsidence and consequently of the marine ingression during the Maastrichtian-Danian, we recognise that flexural subsidence only accounts for ingressions in areas adjacent to the Andean orogen. Therefore, more distal transgressive deposits cannot be entirely attributed to flexural loading. Accommodation farther from the orogenic load may be created by dynamic sub-crustal loads (Gurnis, 1992; Catuneanu et al., 1997, 2004), which depend on the dynamics of mantle flow related to subduction processes (Mitrovica et al., 1989; Gurnis, 1992) and its effect operates at a long-wavelength (up to ~2000 km) (Burgess and Moresi, 1999).

Some predicted effects of dynamic topography in foreland basin systems are subsidence extending cratonward farther from the orogen (Burgess and Moresi, 1999), suppression or diminution of the erosional characteristics of the forebulge, and sedimentation in the forebulge and backbulge depozones (Catuneanu et al., 1997, 2004). In the MAB, particularly for the Magallanes Province and

Tierra del Fuego, Fig. 11 shows that between 70-60 Ma the Manzano and Evans wells (adjacent to the orogenic front) record maximum subsidence while the Condor well (located cratonward) reflects moderate subsidence. Likewise, Náñez and Malumián (2009) and Sachse et al. (2015) highlighted a reduced latest Cretaceous-Paleocene sedimentary thickness (~50 m) over the Rio Chico-Dungeness Arch and Malvinas Basin, which can be interpreted as condensed sections deposited during reduced accommodation conditions. Such a subsidence pattern and distal stratigraphic records match the predicted behaviour for dynamic subsidence acting in a long-wavelength in foreland basins. However, according to Fosdick et al. (2014), the attenuated Patagonian lithosphere of the MAB promoted flexural subsidence that was transmitted great distances cratonward (but was null in the backbulge depozone) and a diminished forebulge uplift. The latter implies that although the moderate subsidence registered cratonward may be explained by the inherent mechanical parameters of the MAB, the ~50 m thick sedimentary packages that accumulated in the most distal depozones might have been facilitated by dynamic subsidence.

On the other hand, Dávila et al. (2019) based on residual subsidence modelling, suggested that during 130-66 Ma additional subcrustal forces were necessary to explain the amount of subsidence observed in the northernmost part of the MAB. Additionally, Gianni et al. (2018) proposed the existence of a large flat slab subduction segment during 75-60 Ma in northern Patagonia, which caused enough dynamic subsidence to tilt areas farthest away from the influence of orogenic loading, thus allowing the Maastrichtian-Danian transgression.

Together, these observations suggest that the Maastrichtian-Danian marine ingression in the MAB was influenced by both flexural subsidence and dynamic subsidence.

5.4 Constraints on the timing of fold-thrust belt deformation

The integration of our dataset with previous structural and sedimentological data allows us to constrain some phases of active deformation in the Southern Patagonian wedge.

Before the late Campanian (~75 Ma), the fold-thrust-belt underwent protracted exhumation of the hinterland source terranes, involving the Tobífera Formation (and equivalents), remnants of the RVB, Paleozoic basement and rapid exhumation of the Cordillera Darwin core (Nelson, 1982; Kohn et al., 1995; Sánchez, 2006; Mpodozis in Álvarez et al., 2006; Romans et al., 2010; McAtamney et al., 2011). By the Maastrichtian (~72-68 Ma), a continuous exhumation of the hinterland gave rise to moderated to accentuated erosion of the arc (Fig. 8) reflected in the modal signature and detrital zircon ages of the younger deposits of the Dorotea and Rocallosa formations (Figs. 6, 7) and equivalent rocks in Tierra del Fuego (see also Torres-Carbonell and Olivero, 2019). Moderate amounts of sedimentary lithics in the younger Dorotea-Rocallosa strata suggest the incorporation of previous foreland deposits into the thrust-belt. Shoaling during the transition between the Tres Pasos-Fuentes to Dorotea-Rocallosa formations within a normal regressive context can be ascribed to increases in sedimentation rates that outpaced accommodation (by subsidence), the aftermath of accentuated erosion in the hinterland. The results of structural studies suggest an orogen-wide basement-involved faulting event (thick-skinned) manifested by crustal basement shortening and internal deformation (e.g., Fosdick et al., 2011; Betka et al., 2015). Altogether, the fold-thrust-belt evolution and sedimentary records in the basin suggest a phase of mainly internal shortening and thickening of the wedge, with limited forelandward advance of the deformation front (Fig. 12a). The latter may suggest that erosion rates outstripped shortening, promoting stability of the orogenic wedge.

The second phase of shortening, between ~68-58 Ma, is characterised by minor exhumation in the hinterland but significant forelandward advance of the thrust front (Fig. 12b), accompanied by considerable erosion of the wedge at least during the Maastrichtian-Danian transition (Sial et al., 2001). Upper Cretaceous foredeep deposits are incorporated into the fold-thrust belt in the Ultima Esperanza and Magallanes Provinces (e.g., Tenerife Thrust of Fosdick et al., 2011; Betka et al., 2015) while thrusting of Maastrichtian-Danian rocks with brittle-ductile deformation under

submarine conditions occurred in Tierra del Fuego (e.g., D1 structures of Torres Carbonell and Olivero, 2019). The forelandward transfer of deformation is evidenced in the sedimentary record by the upward replacement of basement-derived detritus by chert and sedimentary lithics throughout the Maastrichtian-Paleocene strata, portraying a recycled-orogen trend in the Chorrillo Chico Formation (Fig. 7). Moreover, the relative contribution from the RVB, Tobífera Formation and Andean Metamorphic Complexes appear to have decreased by the Paleocene in the Chorrillo Chico and Cabo Nariz beds, suggesting a structurally dammed hinterland. In Tierra del Fuego, progressively coarser sediments trapped adjacent to the orogenic wedge (Torres Carbonell and Olivero, 2019) indicate either a piggyback mode of thrust propagation or out-of-sequence thrusting. These series of thrust-loads caused an ample accommodation suitable for the establishment of estuarine deposits in the Ultima Esperanza Province and deep-marine turbidite sequences in the Magallanes Province and Tierra del Fuego, which correspond to the sedimentological record of the Maastrichtian-Danian transgression in the MAB. The significant forelandward transfer of deformation evidenced during this stage, represents the transition from a thick-skinned to a thin-skinned structural style (Fig. 12b) probably triggered by an increased magnitude of the crustal shortening outpacing erosion rates.

6. CONCLUSIONS

An upward-shallowing cycle during the late Campanian to late Maastrichtian of the MAB is recorded from the Fuentes-Tes Pasos to Rocallosa-Dorotea formations, passing from outer shelf-slope deposits to shoreface-deltaic environments, respectively. From the latest Maastrichtian to Paleocene, a deepening cycle took place represented by estuarine deposits in the uppermost Dorotea Formation and by the deep-water fan system of Chorrillo Chico Formation and Cabo Naríz beds. This deepening cycle, which represents the stratigraphic record of the Maastrichtian-Danian transgression, is apparent in the entire basin.

Our palynological results suggest a cool-temperate to warm-temperate (~6-17°C) palaeoclimate during the Maastrichtian-Danian, consistent with cool marine conditions recorded in

the South Atlantic, which implies no link between the transgression and relative climatic optima. Progressive sea-level fall during the Maastrichtian-Danian suggests that eustasy was not a driver of the marine ingression. The stratigraphic, tectonic, and subsidence evolution of the basin imply that the orogenic loading of the Southern Patagonian Andes was a primary driver of the transgression in the MAB. Additionally, changes in dynamic topography strongly modulated the extent of the continental flooding event.

Modal composition and ~400 detrital zircons U-Pb ages show a continuous input from the RVB remnants, Paleozoic basement, Tobífera Formation, and magmatic arc during deposition of the Rocallosa-Dorotea and Chorrillo Chico-Cabo Naríz formations. The relative contribution from the RVB, Tobífera Formation and Andean Metamorphic complexes appears to have decreased by the Paleocene, suggesting a structurally dammed hinterland or a regional change in the sediment dispersal system.

We envisage two phases of Southern Patagonian orogenic growth. The first phase (prior to ~68 Ma) would have been characterised by internal deformation, thickening of the orogenic wedge, and accentuated hinterland exhumation, with a low magnitude of crustal shortening and high erosion rates that inhibited forelandward advance of the wedge. The second phase (~68-58 Ma) would have been characterised by minor hinterland exhumation and significant forelandward advance of the thrust front, probably triggered by an increased magnitude of crustal shortening.

ACKNOWLEDGEMENTS

This study was financially and logistically supported by FONDECYT projects 1130006 and 1161806 and by the CONICYT-PFCHA-National PhD Scholarship 2017 No. 21170419. L.K. Sánchez and I.A. Gómez (Universidad de Chile) are thanked for their invaluable assistance during field campaigns, A.V. Poblete and L. Celle for support in the palynological and petrographic analysis, respectively. We gratefully acknowledge L. Rojas (Enap-Sipetrol) for permission to review unpublished reports. We thank L. Buatois for his very kind and helpful assistance in the identification

of some ichnological traces, M. Leisen (CEGA), L. Solari (UNAM), M. Suárez and F. Llona (SERNAGEOMIN) are thanked for detrital zircon age dating. We also thank J. Martinod, Theresa Schwartz, David Barbeau Jr., and Matthew Malkowski for helpful comments on an early version of the manuscript. We are grateful to Sarah W.M George and an anonymous reviewer for their constructive and thoughtful reviews and editor Jasper Knight for his excellent editing work.

REFERENCES

Aguirre-Urreta, B., Tunik, M., Naipauer, M., Pazos, P., Ottone, E., Fanning, M., Ramos, V.A., 2011. Malargüe Group (Maastrichtian–Danian) deposits in the Neuquén Andes, Argentina: Implications for the onset of the first Atlantic transgression related to Western Gondwana break-up. Gondwana Research 19, 482-494.

Álvarez, P., Elgueta, S., Mpodozis, C., Briceño, M., Vieytes, H., Radic, J.P., Mella, P., 2006. Revisión de la estratigrafía y facies de la cuenca de antepaís Cretácica entre Lago Argentino y Península Brunswick. Proyecto Tranquilo-Otway, Informe Final. Empresa Nacional de Petróleo (ENAP), Unpublished technical report, 290 pp.

Bann, K.L., Fielding, C.R., 2004. An integrated ichnological and sedimentological comparison of non-deltaic shoreface and subaqueous delta deposits in Permian reservoir units of Australia. In: McIlroy, D. (Ed.), The Application of Ichnology to Palaeoenvironmental and Stratigraphic Analysis. Geological Society of London, Special Publications 228, pp. 273-310.

Barbeau Jr, D.L., Olivero, E.B., Swanson-Hysell, N.L., Zahid, K.M., Murray, K.E., Gehrels, G.E., 2009. Detrital-zircon geochronology of the eastern Magallanes foreland basin: Implications for Eocene kinematics of the northern Scotia Arc and Drake Passage. Earth and Planetary Science Letters 284, 489-503.

Barrera, E., Savin, S.M., 1999. Evolution of late Campanian-Maastrichtian marine climates and oceans. In: Barrera, E., Johnson, C.C. (Eds.), Evolution of the Cretaceous Ocean-Climate System. Geological Society of America, Special Papers 332, pp. 245-282.

Barrio, C.A., 1990. Late Cretaceous-Early Tertiary sedimentation in a semi-arid foreland basin (Neuquén Basin, western Argentina). Sedimentary Geology 66, 255-275.

Betka, P., Klepeis, K., Mosher, S., 2015. Along-strike variation in crustal shortening and kinematic evolution of the base of a retroarc fold-and-thrust belt: Magallanes, Chile 53° S–54°. Geological Society of America Bulletin 127, 1108-1134.

Bhattacharya, J.P., 2010. Deltas. In: James, N.P., Dalrymple, R.W. (Eds.), Facies Models 4. Geological Association of Canada, St. John's Newfoundland and Labrador, pp. 233-264.

Biddle, K.T., Uliana, M.A., Mitchum Jr, R.M., Fitzgerald, M.G., Wright, R.C., 1986. The stratigraphic and structural evolution of the central and eastern Magallanes Basin, southern South America. In: Allen, P.A., Homewood, P. (Eds.), Foreland basins. International Association of Sedimentologists Special Publication 8, pp. 41-61.

Borel, C.M., 2007. Algas no silíceas y acritarcos de depósitos costeros holocenos en el arroyo La Ballenera, Buenos Aires, Argentina. Ameghiniana 44, 359-366.

Bowman, V.C., Francis, J.E., Askin, R.A., Riding, J.B., Swindles, G.T., 2014. Latest Cretaceous–earliest Paleogene vegetation and climate change at the high southern latitudes: palynological evidence from Seymour Island, Antarctic Peninsula. Palaeogeography, Palaeoclimatology, Palaeoecology 408, 26-47.

Buatois, L.A., Mángano, M.G., 2011. Ichnology: Organism-substrate interactions in space and time. Cambridge University Press, Cambridge.

Burgess, P.M., Moresi, L.N., 1999. Modelling rates and distribution of subsidence due to dynamic topography over subducting slabs: is it possible to identify dynamic topography from ancient strata? Basin Research 11, 305-314.

Calderón, M., Fildani, A., Herve, F., Fanning, C.M., Weislogel, A., Cordani, U., 2007. Late Jurassic bimodal magmatism in the northern sea-floor remnant of the Rocas Verdes basin, southern Patagonian Andes. Journal of the Geological Society 164, 1011-1022.

Carrillo-Berumen, R., Quattrocchio, M.E., Helenes, J., 2013. Paleogene continental Palynomorphs of the formations Chorrillo Chico and Agua Fresca, Punta Prat, Magallanes, Chile. Andean Geology 40, 539-560.

Catuneanu, O. 2004. Retroarc foreland systems—evolution through time. Journal of African Earth Sciences 38, 225-242.

Catuneanu, O., Beaumont, C., Waschbusch, P., 1997. Interplay of static loads and subduction dynamics in foreland basins: Reciprocal stratigraphies and the “missing” peripheral bulge. Geology 25, 1087-1090.

Catuneanu, O., Galloway, W.E., Kendall, C.G.S.C., Miall, A.D., Posamentier, H.W., Strasser, A., Tucker, M E., 2011. Sequence stratigraphy: methodology and nomenclature. Newsletters on Stratigraphy 44, 173-245.

Charrier, R., Lahsen, A., 1969. Stratigraphy of Late Cretaceous-Early Eocene, Seno Skyring-Strait of Magellan Area, Magallanes Province, Chile. American Association of Petroleum Geologist Bulletin 53, 568-590.

Covault, J.A., Romans, B.W., Graham, S.A., 2009. Outcrop expression of a continental-margin-scale shelf-edge delta from the Cretaceous Magallanes Basin, Chile. Journal of Sedimentary Research 79, 523-539.

Cramer, B.S., Toggweiler, J.R., Wright, J.D., Katz, M.E., Miller, K.G., 2009. Ocean overturning since the Late Cretaceous: Inferences from a new benthic foraminiferal isotope compilation. Paleoceanography 24, PA4216. https://doi.org/10.1029/2008PA001683

Cross, T.A., Pilger Jr, R.H., 1978. Tectonic controls of Late Cretaceous sedimentation, western interior, USA. Nature 274, 653-657.

Dalrymple, R.W., Zaitlin, B.A., Boyd, R., 1992. Estuarine facies models: conceptual basis and stratigraphic implications. Journal of Sedimentary Petrology 62, 1130-1146.

Dalziel, I.W.D., 1981. Back-arc extension in the southern Andes: a review and critical reappraisal. Philosophical Transactions of the Royal Society of London. Series A, Mathematical and Physical Sciences 300, 319-335.

Daniels, B.G., Hubbard, S.M., Romans, B.W., Malkowski, M.A., Matthews, W.A., Bernhardt, A., Fildani, A., Graham, S.A., 2019. Revised chronostratigraphic framework for the Cretaceous Magallanes-Austral Basin, Última Esperanza Province, Chile. Journal of South American Earth Sciences 94, 102209. https://doi.org/10.1016/j.jsames.2019.05.025

Dávila, F.M., Ávila, P., Martina, F., 2019. Relative contributions of tectonics and dynamic topography to the Mesozoic-Cenozoic subsidence of southern Patagonia. Journal of South American Earth Sciences 93, 412-423.

Dickinson, W.R., 1985. Interpreting provenance relations from detrital modes of sandstones. In: Zuffa, G. (Ed.), Provenance of arenites. Springer, Dordrecht, pp. 333-361.

Dickinson, W.R., Gehrels, G.E., 2009. Use of U–Pb ages of detrital zircons to infer maximum depositional ages of strata: a test against a Colorado Plateau Mesozoic database. Earth and Planetary Science Letters 288, 115-125.

Dott Jr, R.H., Bourgeois, J., 1982. Hummocky stratification: significance of its variable bedding sequences. Geological Society of America Bulletin 93, 663-680.

Dumas, S., Arnott, R.W., 2006. Origin of hummocky and swaley cross-stratification—The controlling influence of unidirectional current strength and aggradation rate. Geology 34, 1073-1076.

Falk, P.D., Dorsey, R.J., 1998. Rapid development of gravelly high-density turbidity currents in marine Gilbert-type fan deltas, Loreto Basin, Baja California Sur, Mexico. Sedimentology 45, 331-349.

Fildani, A., Cope, T.D., Graham, S.A., Wooden, J.L., 2003. Initiation of the Magallanes foreland basin: Timing of the southernmost Patagonian Andes orogeny revised by detrital zircon provenance analysis. Geology 31, 1081-1084.

Fildani, A., Hessler, A.M., 2005. Stratigraphic record across a retroarc basin inversion: Rocas Verdes–Magallanes basin, Patagonian Andes, Chile. Geological Society of America Bulletin 117, 1596-1614.

Flemming, B.W., 2000. A revised textural classification of gravel-free muddy sediments on the basis of ternary diagrams. Continental Shelf Research 20, 1125-1137.

Fosdick, J.C., Romans, B.W., Fildani, A., Bernhardt, A., Calderón, M., Graham, S.A., 2011. Kinematic evolution of the Patagonian retroarc fold-and-thrust belt and Magallanes foreland basin, Chile and Argentina, 51 30′ S. Geological Society of America Bulletin 123, 1679-1698.

Fosdick, J.C., Graham, S.A., Hilley, G.E., 2014. Influence of attenuated lithosphere and sediment loading on flexure of the deep-water Magallanes retroarc foreland basin, Southern Andes, Tectonics 33, 2505–2525.

Fosdick, J.C., Grove, M., Graham, S.A., Hourigan, J.K., Lovera, O., Romans, B.W., 2015. Detrital thermochronologic record of burial heating and sediment recycling in the Magallanes foreland basin, Patagonian Andes. Basin Research 27, 546-572.

George, S.W., Davis, S.N., Fernández, R.A., Manríquez, L.M., Leppe, M.A., Horton, B.K., Clarke, J.A., 2020. Chronology of deposition and unconformity development across the Cretaceous–Paleogene boundary, Magallanes-Austral Basin, Patagonian Andes. Journal of South American Earth Sciences, 102237, https://doi.org/10.1016/j.jsames.2019.102237

Gianni, G.M., Dávila, F., Echaurren, A., Fennell, L., Tobal, J., Navarrete, C.R., Quezada, P., Folguera, A., Giménez, M., 2018. A geodynamic model linking Cretaceous orogeny, arc migration, foreland basin subsidence and marine ingression in southern South America. Earth-Science Reviews 185, 437-462.

Guler, M.V., Estebenet, M.S.G., Navarro, E.L., Astini, R.A., Panera, J.P.P., Ottone, E.G., Paolillo, M.A., 2019. Maastrichtian to Danian Atlantic transgression in the north of Patagonia: A dinoflagellate cyst approach. Journal of South American Earth Sciences 92, 552-564.

Gutiérrez, N.M., Le Roux, J.P., Vásquez, A., Carreño, C., Pedroza, V., Araos, J., Rivera, H.A., Hinojosa, L.F. 2017. Tectonic events reflected by palaeocurrents, zircon geochronology, and palaeobotany in the Sierra Baguales of Chilean Patagonia. Tectonophysics 695, 76-99.

Haq, B.U., 2014. Cretaceous eustasy revisited. Global and Planetary Change 113, 44-58.

Haughton, P., Davis, C., McCaffrey, W., Barker, S., 2009. Hybrid sediment gravity flow deposits–classification, origin and significance. Marine and Petroleum Geology 26, 1900-1918.

Hernández, R.M., Jordan, T.E., Farjat, A.D., Echavarría, L., Idleman, B.D., Reynolds, J.H., 2005. Age, distribution, tectonics, and eustatic controls of the Paranense and Caribbean marine transgressions in southern Bolivia and Argentina. Journal of South American Earth Sciences 19, 495-512.

Herngreen, G.F.W., Kedves, M., Rovnina, L.V., Smirnova, S.B. 1996. Cretaceous palynofloral provinces: a review. In: Jansonius, J., McGregor, D.C. (Eds.), Palynology: Principles and Applications. American Association of Stratigraphic Palynologists Foundation, pp. 1157-1188.

Hervé, F., Fanning, C.M., Pankhurst, R.J., 2003. Detrital zircon age patterns and provenance of the metamorphic complexes of southern Chile. Journal of South American Earth Sciences 16, 107-123.

Hervé, F., Pankhurst, R.J., Fanning, C.M., Calderón, M., Yaxley, G.M., 2007. The South Patagonian batholith: 150 my of granite magmatism on a plate margin. Lithos 97, 373-394.

Hervé, F., Fanning, C.M., Pankhurst, R.J., Mpodozis, C., Klepeis, K., Calderón, M., Thomson, S.N., 2010. Detrital zircon SHRIMP U–Pb age study of the Cordillera Darwin Metamorphic Complex of Tierra del Fuego: sedimentary sources and implications for the evolution of the Pacific margin of Gondwana. Journal of the Geological Society 167, 555-568.

Ingersoll, R.V., Bullard, T.F., Ford, R.L., Grimm, J.P., Pickle, J.D., Sares, S.W., 1984. The effect of grain size on detrital modes: a test of the Gazzi-Dickinson point-counting method. Journal of Sedimentary Research 54, 103-116.

Kamola, D.L., Huntoon, J E., 1995. Repetitive stratal patterns in a foreland basin sandstone and their possible tectonic significance. Geology 23, 177-180.

Kohn, M.J., Spear, F.S., Harrison, T.M., Dalziel, I.W.D., 1995. $^{40}Ar/^{39}Ar$ geochronology and P-T-t paths from the Cordillera Darwin metamorphic complex, Tierra del Fuego, Chile. Journal of Metamorphic Geology 13, 251-270.

Klepeis, K., Betka, P., Clarke, G., Fanning, M., Hervé, F., Rojas, L., Mpodozis, C., Thomson, S., 2010. Continental underthrusting and obduction during the Cretaceous closure of the Rocas Verdes rift basin, Cordillera Darwin, Patagonian Andes. Tectonics 29, TC3014. doi:10.1029/2009TC002610.

Le Roux, J.P., 2012. A review of Tertiary climate changes in southern South America and the Antarctic Peninsula. Part 1: Oceanic conditions. Sedimentary Geology 247, 1-20.

Le Roux, J.P., Nielsen, S.N., Henríquez, A., 2008. Depositional environment of *Stelloglyphus llicoensis* isp. nov.: a new radial trace fossil from the Neogene Ranquil Formation, south-central Chile. Andean Geology 35, 307-320.

Le Roux, J.P., Puratich, J., Mourgues, F.A., Oyarzún, J.L., Otero, R.A., Torres, T., Hervé, F., 2010. Estuary deposits in the Río Baguales Formation (Chattian-Aquitanean), Magallanes Province, Chile. Andean Geology 37, 329-344.

Lowe, D.R., 1982. Sediment gravity flows; II, Depositional models with special reference to the deposits of high-density turbidity currents. Journal of Sedimentary Research 52, 279-297.

Macellari, C.E., Barrio, C.A., Manassero, M.J., 1989. Upper Cretaceous to Paleocene depositional sequences and sandstone petrography of southwestern Patagonia (Argentina and Chile). Journal of South American Earth Sciences 2, 223-239.

Mahon, K.I., 1996. The New "York" regression: Application of an improved statistical method to geochemistry. International Geology Review 38, 293-303.

Malkowski, M.A., Grove, M., Graham, S.A., 2016. Unzipping the Patagonian Andes—Long-lived influence of rifting history on foreland basin evolution. Lithosphere 8, 23-28.

Malkowski, M.A., Sharman, G.R., Graham, S.A., Fildani, A., 2017a. Characterisation and diachronous initiation of coarse clastic deposition in the Magallanes–Austral foreland basin, Patagonian Andes. Basin Research 29, 298-326.

Malkowski, M.A., Schwartz, T.M., Sharman, G.R., Sickmann, Z.T., Graham, S.A., 2017b. Stratigraphic and provenance variations in the early evolution of the Magallanes-Austral foreland basin: Implications for the

role of longitudinal versus transverse sediment dispersal during arc-continent collision. GSA Bulletin 129, 349-371.

Malkowski, M.A., Jobe, Z.R., Sharman, G.R., Graham, S.A., 2018. Down-slope facies variability within deep-water channel systems: Insights from the Upper Cretaceous Cerro Toro Formation, southern Patagonia. Sedimentology 65, 1918-1946.

Malumián, N., Caramés, A., 1997. Upper Campanian-Paleogene from the Río Turbio coal measures in southern Argentina: micropaleontology and the Paleocene/Eocene boundary. Journal of South American Earth Sciences 10, 189-201.

Malumián, N., Nanez, C., 2011. The Late Cretaceous–Cenozoic transgressions in Patagonia and the Fuegian Andes: foraminifera, palaeoecology, and palaeogeography. Biological Journal of the Linnean Society 103, 269-288.

Manríquez, L.M., Lavina, E.L., Fernández, R.A., Trevisan, C., Leppe, M.A., 2019. Campanian-Maastrichtian and Eocene stratigraphic architecture, facies analysis, and paleoenvironmental evolution of the northern Magallanes Basin (Chilean Patagonia). Journal of South American Earth Sciences 93, 102-118.

Marenssi, S., Guler, V., Casadío, S., Guerstein, R., Papú, O., 2004. Sedimentology and palynology of the Calafate Formation (Maastrichtian), Austral Basin, Southern Patagonia, Argentina. Cretaceous Research 25, 907-918.

Martinioni, D.R., Olivero, E.B., Medina, F.A., Palamarczuk, S.C., 2013. Cretaceous stratigraphy of Sierra de Beauvoir, Fuegian Andes, Argentina. Revista de la Asociación Geológica Argentina 70, 70-95.

McAtamney, J., Klepeis, K., Mehrtens, C., Thomson, S., Betka, P., Rojas, L., Snyder, S., 2011. Along-strike variability of back-arc basin collapse and the initiation of sedimentation in the Magallanes foreland basin, southernmost Andes (53–54.5° S). Tectonics 30, TC5001. https://doi.org/10.1029/2010TC002826

MacDonald, D.I., 1986. Storm-generated sandstone beds from the Upper Cretaceous of south Chile and their regional significance. Andean Geology 28, 69-76.

MacEachern, J.A., Bann, K.L., Bhattacharya, J.P., Howell Jr, C.D., 2005. Ichnology of deltas: organism responses to the dynamic interplay of rivers, waves, storms, and tides. In: Giosan L., Bhattacharya, J.P. (Eds.), River deltas: concepts, models and examples. SEPM Special Publications 83, pp. 1-37.

Mella, P., Sánchez, J., 2000. Modelación cuantitativa de la subsidencia tectónicaen el extremo sur de la Cuenca Austral, XII Región-Chile. IX Congreso Geológico Chileno. Puerto Varas, Chile, pp. 221-225.

Miall, A.D. 2014. Fluvial depositional systems. Springer, Berlin.

Mpodozis, C., Mella, P., Padva, D., 2011. Estratigrafía y megasecuencias sedimentarias en la cuenca Austral-Magallanes, Argentina y Chile. VII Congreso de Exploración y Desarrollo de Hidrocarburos, Simposio Cuencas Argentinas: visión actual, pp. 97-137.

Myrow, P.M., Fischer, W., Goodge, J.W. 2002. Wave-modified turbidites: combined-flow shoreline and shelf deposits, Cambrian, Antarctica. Journal of Sedimentary Research 72, 641-656.

Náñez, C., Malumián, N., 2008. Paleobiogeografía y paleogeografía del Maastrichtiense marino de la Patagonia, Tierra del Fuego y la Plataforma Continental Argentina, según sus foraminíferos bentónicos. Revista Española de Paleontología 23, 273-300.

Nelson, E.P., 1982. Post-tectonic uplift of the Cordillera Darwin orogenic core complex: evidence from fission track geochronology and closing temperature–time relationships. Journal of the Geological Society 139, 755-761.

Odino Barreto, A.L., Cereceda, A., Gómez Peral, L., Coronel, M.D., Tettamanti, C., Poire, D.G., 2018. Sedimentology of the shallow marine deposits of the Calafate Formation during the Maastrichtian transgression at Lago Argentino, Austral-Magallanes Basin, Argentina. Latin American Journal of Sedimentology and Basin Analysis 25,169-191.

Olariu, C., Bhattacharya, J.P., 2006. Terminal distributary channels and delta front architecture of river-dominated delta systems. Journal of Sedimentary Research 76, 212-233.

Olivero, E.B., Malumián, N., Palamarczuk, S., 2003. Estratigrafía del Cretácico Superior-Paleoceno del área de Bahía Thetis, Andes fueguinos, Argentina: acontecimientos tectónicos y paleobiológicos. Andean Geology 30, 245-263.

Palma-Heldt, S., 1983. Estudio palinológico del Terciario sedimentario de Lonquimay, provincia de Malleco, Chile. Andean Geology 18, 55-75.

Pankhurst, R.J., Riley, T.R., Fanning, C.M., Kelley, S.P., 2000. Episodic silicic volcanism in Patagonia and the Antarctic Peninsula: chronology of magmatism associated with the break-up of Gondwana. Journal of Petrology 41, 605-625.

Plink-Björklund, P., Hampson, G.J., Steel, R.J., Burgess, P.M., Dalrymple, R.W., 2008. Wave-to-tide facies change in a Campanian shoreline complex, Chimney Rock Tongue, Wyoming-Utah, USA. In: Hampson, G.J., Steel, R.J., Burgess, P.M.; Dalrymple, R.W. (Eds.), Recent advances in models of shallow-marine stratigraphy. SEPM Special Publication 90, pp. 265-291.

Povilauskas, L., 2017. Palynostratigraphy of the Cretaceous–Paleogene in the Austral basin, SW Santa Cruz Province, Argentina. Revista Brasileira de Paleontología 20, 299-320.

Quattrocchio, M.E., Martínez, M.A., Pavisich, A.C., Volkheimer, W., 2006. Early Cretaceous palynostratigraphy, palynofacies and palaeoenvironments of well sections in northeastern Tierra del Fuego, Argentina. Cretaceous Research 27, 584-602.

Rapalini, A E., Calderón, M., Singer, S., Hervé, F., Cordani, U., 2008. Tectonic implications of a paleomagnetic study of the Sarmiento Ophiolitic Complex, southern Chile. Tectonophysics 452, 29-41.

Reinson, G.E., 1992. Transgressive barrier island and estuarine systems. In: Walker, R.G., James, N.P. (Eds.), Facies Models: Response to Sea Level Changes. Geological Association of Canada, St. Johns, Newfoundland and Labrador, pp. 179-194.

del Río, C.J., Martínez, S.A., 2015. Paleobiogeography of the Danian molluscan assemblages of Patagonia (Argentina). Palaeogeography, Palaeoclimatology, Palaeoecology 417, 274-292.

Rivera, H.A., 2017. Insights into the tectonostratigraphic evolution of the Southern Magallanes Basin, Southern Chile, during the Cenozoic. (Master's thesis) Universidad de Chile, Santiago, Chile, 149 pp.

Rivera, H.A., Le Roux, J.P., Sánchez, L.K., Mariño-Martínez, J.E., Salazar, C., Barragán, J.C., 2018. Palaeoredox conditions and sequence stratigraphy of the Cretaceous storm-dominated, mixed siliciclastic-carbonate ramp in the Eastern Cordillera Basin (Colombia): Evidence from sedimentary geochemical proxies and facies analysis. Sedimentary Geology 372, 1-24.

Roddaz, M., Hermoza, W., Mora, A., Baby, P., Parra, M., Christophoul, F., Espurt, N., 2010. Cenozoic sedimentary evolution of the Amazonian foreland basin system. In: Hoorn, C., Wesselingh, E.P. (Eds.), Amazonia, Landscape and Species Evolution: A Look into the Past. Blackwell-Wiley, Hoboken, pp. 61-88.

Rojas, E., Le Roux, J.P., 2005. Sedimentary processes on a Gilbert-type delta in Lake Llanquihue, southern Chile. Andean Geology 32, 19-31.

Romans, B.W., Hubbard, S.M., Graham, S.A., 2009. Stratigraphic evolution of an outcropping continental slope system, Tres Pasos Formation at Cerro Divisadero, Chile. Sedimentology 56, 737-764.

Romans, B.W., Fildani, A., Graham, S.A., Hubbard, S.M., Covault, J.A., 2010. Importance of predecessor basin history on the sedimentary fill of a retroarc foreland basin: provenance analysis of the Cretaceous Magallanes basin, Chile (50-52 S). Basin Research 22, 640-658.

Rossi, V.M., Steel, R.J., 2016. The role of tidal, wave and river currents in the evolution of mixed-energy deltas: Example from the Lajas Formation (Argentina). Sedimentology 63, 824-864.

Rossignol, C., Hallot, E., Bourquin, S., Poujol, M., Jolivet, M., Pellenard, P., Dabard, M.P., 2019. Using volcaniclastic rocks to constrain sedimentation ages: To what extent are volcanism and sedimentation synchronous? Sedimentary Geology 381, 46-64.

Sachse, V.F., Strozyk, F., Anka, Z., Rodriguez, J.F., Di Primio, R., 2016. The tectono-stratigraphic evolution of the Austral Basin and adjacent areas against the background of Andean tectonics, southern Argentina, South America. Basin Research 28, 462-482.

Sánchez, A., 2006. Proveniencia sedimentaria de estratos de Cabo Naríz y Formación Cerro Toro, Cretácico Tardío-Paleoceno, Magallanes, Chile. (Master's thesis), Universidad de Chile, Santiago, Chile, 153 pp.

Sánchez, A., Pavlishina, P., Godoy, E., Herve, F., Fanning, C.M., 2010. On the presence of Upper Paleocene rocks in the foreland succession at Cabo Nariz, Tierra del Fuego, Chile: geology and new palynological and U-Pb data. Andean Geology 37, 413-432.

Scasso, R.A., Aberhan, M., Ruiz, L., Weidemeyer, S., Medina, F.A., Kiessling, W., 2012. Integrated bio-and lithofacies analysis of coarse-grained, tide-dominated deltaic environments across the Cretaceous/Paleogene boundary in Patagonia, Argentina. Cretaceous Research 36, 37-57.

Shultz, M.R., Fildani, A., Cope, T.D., Graham, S.A., 2005. Deposition and stratigraphic architecture of an outcropping ancient slope system: Tres Pasos Formation, Magallanes Basin, southern Chile. In: Hodgson, D.M., Flint, S.S. (Eds.), Submarine Slope Systems: Processes and Products. Geological Society of London, Special Publications 244, pp. 27-50.

Schwartz, T.M., Graham, S.A., 2015. Stratigraphic architecture of a tide-influenced shelf-edge delta, Upper Cretaceous Dorotea Formation, Magallanes-Austral Basin, Patagonia. Sedimentology 62, 1039-1077.

Schwartz, T.M., Fosdick, J.C., Graham, S.A., 2017. Using detrital zircon U-Pb ages to calculate Late Cretaceous sedimentation rates in the Magallanes-Austral basin, Patagonia. Basin Research 29, 725-746.

Sial, A.N., Ferreira, V.P., Toselli, A.J., Parada, M.A., Acenolaza, F.G., Pimentel, M.M., Alonso, R.N., 2001. Carbon and oxygen isotope compositions of some Upper Cretaceous–Paleocene sequences in Argentina and Chile. International Geology Review 43, 892-909.

Stern, C.R., Mohseni, P.P., Fuenzalida, P.R., 1991. Petrochemistry and tectonic significance of lower Cretaceous Barros Arana Formation basalts, southernmost Chilean Andes. Journal of South American Earth Sciences 4, 331-342.

Thomas, C.R., 1949. Geology and petroleum exploration in Magallanes Province, Chile. AAPG Bulletin 33, 1553-1578.

Thomas, R.G., Smith, D.G., Wood, J.M., Visser, J., Calverley-Range, E.A., Koster, E.H., 1987. Inclined heterolithic stratification—terminology, description, interpretation and significance. Sedimentary Geology 53, 123-179.

Torres Carbonell, P.J., Olivero, E.B., 2019. Tectonic control on the evolution of depositional systems in a fossil, marine foreland basin: Example from the SE Austral Basin, Tierra del Fuego, Argentina. Marine and Petroleum Geology 104, 40-60.

Uliana, M.A., Biddle, K.T., 1988. Mesozoic-Cenozoic paleogeographic and geodynamic evolution of southern South America. Revista Brasileira de Geociencias 18, 172-190.

Vellekoop, J., Holwerda, F., Prámparo, M.B., Willmott, V., Schouten, S., Cúneo, N.R., Scasso, R., Brinkhuis, H., 2017. Climate and sea-level changes across a shallow marine Cretaceous–Palaeogene boundary succession in Patagonia, Argentina. Palaeontology 60, 519-534.

Vermeesch, P., 2004. How many grains are needed for a provenance study? Earth and Planetary Science Letters 224, 351-441.

Wilson, T.J., 1991. Transition from back-arc to foreland basin development in the southernmost Andes: Stratigraphic record from the Ultima Esperanza District, Chile. Geological Society of America Bulletin 103, 98-111.

Yang, Y., Miall, A.D., 2008. Marine transgressions in the mid-Cretaceous of the Cordilleran foreland basin re-interpreted as orogenic unloading deposits. Bulletin of Canadian Petroleum Geology 56, 179-198.

Zaitlin, B.A., Dalrymple, R.W., Boyd, R.O., 1994. The stratigraphic organization of incised-valley systems associated with relative sea-level change. In: Dalrymple, R.W., Boyd, R.J., Zaitlin, B.A. (Eds.), Incised valley systems: Origin and Sedimentary Sequences. SEPM Special Publications 51, pp. 45-60.

FIGURE CAPTIONS

Figure 1. (a) Simplified morphotectonic map of the Magallanes-Austral Basin (modified from Fildani and Hessler, 2005), showing potential source terranes to the basin. The inset map shows the Maastrichtian-Danian ocean flooding Patagonian basins: (1) Magallanes-Austral, (2) Malvinas, (3) Golfo San Jorge, (4) Cañadón Asfalto, (5) Península Valdes-Rawson, (6) Colorado, (7) Neuquén, (8) Salado. (b) Stratigraphic correlation chart of the studied units, sea-level curve (Haq, 2014), and $\delta^{18}O$ record of South Atlantic foraminifera (Cramer et al., 2009).

Figure 2. (a) Geographical distribution of study areas and other locations mentioned in the text. (1) Manzano well, (2) Evans well, (3) Cóndor well. (b) Geological units, sections, and samples in the Ultima Esperanza Province, (c) Skyring Sound, and (d) Brunswick Peninsula areas within the Magallanes Province. $^{\alpha}$ Fosdick et al., 2015; $^{\beta}$ Hervé et al., 2004; $^{\delta}$ Alvarez et al., 2006.

Figure 3. Measured stratigraphic sections with facies associations, palaeocurrents, and sampled intervals. (a) Stratigraphic columns of the Fuentes, Rocallosa, and Chorrillo Chico formations in the Magallanes Province. (b) Stratigraphic columns of the Dorotea Formation in the Ultima Esperanza Province. The column of La Pesca Bay is modified from Elgueta (in Álvarez et al., 2006). For the location, see Fig. 2.

Figure 4. (a) Slump structures in the Fuentes Formation. (b) Amalgamated beds of hummocky and swaley cross-stratification of FA4. (c) Swaley cross-stratification in FA4. (d) Example of mudstone/sandstone blocks in FA7. (e) Shell lag and wave ravinement surface (Wrs) on the fluvial channels marking the start of TST in section Cerro Pelario. (f) Close-up of shells and bivalve molds. (g) Herringbone and bidirectional cross-stratification in estuary deposits (FA8), section Sierra Dorotea. (h) Tangential, cross-bedding with reactivation surfaces and tidal bundles. (i)

Example of low-angle inclined heterolithic units overlain by tidal creek channels in FA8b. (j) Close-up of heterolithic facies. (k) Plan view of contorted bedding in the Chorrillo Chico Formation in section Rio Blanco. (l) Bouma sequence in turbidite deposits of the FA9. Jacob's staff divisions each 10 cm.

Figure 5. Sandstone framework of the formations studied. (a) Cobble of Member D of the Rocallosa Formation showing (inset) abundant reworked glauconite (Gl) grains, volcanic lithics, and altered K-feldspar (Fk). (b) Microcline grain with exsolution textures. (c) Micaceous schist lithic fragment. (d) Polycrystalline quartz fragment of metamorphic origin. (e) Pelitic sedimentary lithic fragments (Ls). (f) Abundant felsitic (Lvf) volcanic lithic and some plutonic lithic fragments (Lp). (g) Polycrystalline quartz (Qp), felsitic (Lvf) volcanic lithic, metamorphic lithic (Lm) grains. Note siliceous protolith of the metamorphic lithic fragments. (h) Example of microlitic (Lvm) texture with palagonite filling (partly) vesicles of a basalt fragment. (i) Lathwork texture (Lvlt) of volcanic lithic, suggesting the input of mafic rocks. (j) Devitrified felsitic volcanic lithic in the Chorrillo Chico Formation, suggesting a contribution from the Tobífera Formation. (k) Vitric shards (Vs), glauconite, and angular crystals of quartz. Scale bar is 0.5 mm.

Figure 6. Detrital zircon U-Pb geochronology results. (a) Composite histograms and probability plots from the Rocallosa Formation, Cabo Nariz beds (Sánchez et al., 2010), and Chorrillo Chico Formation. Lower case "n" refers to the total number of grains in each sample; potential source terranes are indicated in the inset box. (b) Maximum depositional age calculations for each sample. Accept. MSWD after Mahon (1996). (c) Comparison of the relative proportions of two age groups in different parts of the Magallanes-Austral Basin: Tobifera Fm and basement versus magmatic arc and recycled deposits. Note how Tobifera Fm and basement proportions decrease systematically in the Paleocene samples indicating a regional shift in sediment dispersal system.

Figure 7. Q-F-L and Qm-F-Lt ternary plots displaying detrital modes for the Rocallosa-Dorotea, Cabo Nariz, and Chorrillo Chico Formations. Tectonic provenance fields from Dickinson

(1985); polygons represent univariate confidence intervals. Note the unroofing trend in the Chorrillo Chico Formation and between the Dorotea (northern samples of Romans et al., 2010), and Dorotea-Rocallosa formations (southern samples of this study).

Figure 8. Light transmitted images of selected terrestrial palynomorph specimens from the Rocallosa Formation. (a) *Granatisporites* sp. (b) *Multicellaesporites* sp. (c) *Nothofagidites brassii* type. (d) *Nothofagidites dorotensis*. (e) *Nothofagidites cincta*. (f) *Laevigatosporites vulgaris*. (g) *Clavifera triplex*. (h) *Podocarpidites otagoensis*. (i) *Botryococcus braunii*. Scale is 10 µm.

Figure 9. Schematic diagrams of the interpreted sedimentary environments for the Fuentes, Dorotea, Rocallosa and Chorrillo Chico Formations. (a) Before the Maastrichtian-Danian transgression, a wave-influenced delta (Dorotea Formation) existed in the Ultima Esperanza Province while in the Magallanes Province shoreface environments dominated (Rocallosa Formation). Note that the Fuentes Formation is represented by outer shelf to slope environments. (b) During the transgression, an estuary system developed as filling of incised valley systems in the Ultima Esperanza Province, while in the Magallanes Province is characterised by prograding deep-water turbidite fans (Chorrillo Chico Formation). (c) Palaeocurrent distribution for each studied formation.

Figure 10. (a) Idealised sequence stratigraphic model along-strike the Magallanes-Austral Basin. (b) Sequence stratigraphic framework interpreted for the uppermost Tres Pasos-Dorotea Formations in the Ultima Esperanza Province (b) and the uppermost Fuentes, Rocallosa, and Chorrillo Chico formations in the Magallanes Province (c). LST=lowstand systems tract; HST=highstand systems tract; TST=transgressive systems tract. Location of idealised transect in Fig. 2a.

Figure 11. Tectonic subsidence curves for the Manzano, Evans, and Cóndor wells (see Fig. 2a for location). Note accelerated subsidence in the Manzano, and Evans wells located adjacent to the orogenic front and minimal subsidence in the well situated near to the "forebulge" area during the Maastrichtian-Danian.

Figure 12. Simplified palaeogeographic/palaeotectonic reconstruction and schematic structural configuration (modified from Fosdick et al., 2015) of the Southern Patagonian wedge. (a) The thick-skinned deformation phase, characterised by accentuated hinterland exhumation, internal thickening, shoaling of environments and stalling of the deformation front. (b) The thin-skinned deformation phase, characterised by minor hinterland exhumation, recycled foreland deposits, deepening of environments and significant forelandward advance of the deformation front. Note that palaeogeographic maps are not palinspastically restored and diagrams are not to scale.

TABLE CAPTIONS

Table 1. List of measured stratigraphic sections studied and their geographic distribution along the basin strike. For the geographical location, see Fig. 2.

Table 2. Characteristic facies and interpreted sedimentary processes of the studied units in the Magallanes-Austral Basin. BI=bioturbation index.

Table 3. Summary of palynomorph taxa recorded in the Rocallosa Formation with botanical affinities and palaeoclimatic significances. CT= cool temperate (6-12°C), WT= warm temperate (12-17°C).

APPENDICES

Appendix A. Complementary sedimentary structures and distinctive trace fossils of the facies associations.

Appendix B. Point-count raw results and equations for recalculated Q-F-L and Qm-F-Lt plots.

Appendix C. Detailed mineral separation techniques, and analytical procedures of detrital zircon U-Pb analyses, maximum depositional age calculations, probability density plots and Wetherill Concordia diagrams of the samples.

Appendix D. Detrital zircon U-Pb geochronological analyses from LA-ICP-MS and LA-MC-ICP-MS.

Declaration of interests

☒ The authors declare that they have no known competing financial interests or personal relationships that could have appeared to influence the work reported in this paper.

☐The authors declare the following financial interests/personal relationships which may be considered as potential competing interests:

Section Name	Abbreviated Name	Formation studied	Location
Sierra Dorotea	**SD**	Dorotea	Última Esperanza Province
Demaistre	**DM**		
Cerro Pelario	**CP**		
Punta Eulogio	**PE**	Rocallosa	Magallanes Province
Punta Rocallosa	**PR**		
Punta Canelos	**PC**	Chorrillo Chico	
Punta Prat	**PP**	Rocallosa-Chorrillo Chico	
Fuerte Bulnes-Puerto del Hambre	**BH**	Rocallosa	
Río Blanco	**RB**	Chorrillo Chico	

Code	Lithology	Sedimentary structures	Geometry–contacts–thickness	Fossils – Bioturbation	Sedimentary processes
Fh	Light- to greenish-grey shales and silty shales; carbonaceous or coaly paper shales.	Finely laminated to fissile; normally graded from silt to laminated shales; slump and contorted bedding.	Tabular – Sharp, planar to undulate (wavy) contacts – 15 cm up to 1m.	Rare fossils; (BI=0-2) *Chondrites* isp., *Phycosiphon incertum ?*, *Planolites* isp., and rarerly *Bergaueria* isp., *Zoophycus* isp.	Deposition by suspension and vertical settling in very low- to moderated-energy and poorly-oxygenated environments, below storm-wave base; or in quiet, low-energy environments with abundant organic material supply and undisturbed by current energy.
Fm	Light-black to greyish mudstones.	Massive to vaguely laminated.	Tabular – sharp and planar contacts – up to 10's m.	Rare fossils; (BI=2-3) *Phycodes* isp., *Stelloglyphus llicoensis*, *Palaeophycos* isp., *Cladichnus* cf. *fischeri*, and *Phoebichnus bosoensis*, *Planolites* isp., *Taenidium* isp., *Chondrites* isp.	Deposition by suspension and fast vertical settling in a very low-to-moderated-energy environment, below storm-wave base. In some cases, structureless appearance can be by bioturbation.
Slm	Tan, and greyish siltstones, and very fine-grained sandstone.	Massive to vaguely laminated; normally graded.	Tabular – Sharp-gradual, planar to undulate (wavy) contacts – 15 cm up to 90 cm	Null fossils; (BI=0-1) *Cylindrichnus* isp., horizontal and vertical unidentified trace fossils.	Sedimentation by fast vertical settling in a low-to-moderated-energy environment.
Slh	Beige to pale yellow, buff (weathered) siltstones.	Horizontal laminated, wispy laminated.	Tabular – Sharp, planar to undulate (wavy) contacts – 15 to 50 cm, up to 1 m.	Null fossils; (BI=0-1) horizontal and vertical unidentified trace fossils.	Sedimentation by suspension and vertical settling in a low-to-moderated-energy environment with alternating low and moderate current intensity on the seafloor.
Hlh	Rhythmic intercalations of pale siltstones, very fine-grained sandstones, and reddish mudstones.	Horizontal to low-angle laminated, tidal rythmites; lenticular bedding.	Tabular– sharp contacts—sets of up to 3 m.	Pervasive bioturbation (BI=4-5).	Fluctuations in strength and suspended sediment supply, likely reflecting seasonally or climatic controls, typically associated with a tidal regime.

Sm	Tan, whitish to green, and greyish very fine-to-very coarse-grained (glauconitic or shell-rich) sandstones.	Massive or crudely graded; amalgamated; poorly bedded.	Sub-tabular to tabular, lenticular–sharp and planar contacts, or erosive base–10 cm up to 10's m.	Lenticular bodies with highly fragmented bivalves, gastropods, and oysters. Shell, pebble or mudstone lag deposits on erosional contacts; (BI=0-5) *Thalassinoides* isp., *Cylindrichnus* isp., horizontal unidentified trace fossils.	Rapid accumulation of sand from sediment gravity flows or under conditions of rapid flows carpet shear (fraction-carpet); fast accumulation of sand and shell in channels by high-energy events. Structureless appearance also can be related to bioturbation.
Sw	Beige, buff (weathered) fine-to-medium-grained sandstones.	Symmetrical and asymmetrical wave ripples, undulate lamination; slightly contorted lamination.	Tabular–sharp and planar base, rippled top surface –30 cm up to 50 cm.	Null fossils; (BI=0-2) horizontal and vertical unidentified trace fossils.	Oscillatory and combined flows in shallow waters with bottom friction; alternating traction currents in lower flow regime with vertical accretion processes.
Sr	Pale yellow, light grey very fine-to-fine-grained sandstone.	Current ripples	Tabular– sharp contacts– 30 cm up to 1 m.	Null fossils; in a few cases, mottled texture (BI=4-6).	Deposition of migrating bedforms under unidirectional currents and lower flow regime.
Shcs	Fine-to-medium-grained sandstones; commonly with pebble lag.	Amalgamated or isolated hummocky, and swaley cross-stratification/lamination.	Tabular, amalgamated–sharp or erosive base and gradual top–20 cm up to 60 cm.	Plant or carbonaceous debris; (BI=0-1).	Deposition by combined oscillatory and unidirectional currents well above storm wave-base and near fair-weather wave-base.
Spl	Grey to greenish, fine-to-medium-grained sandstones.	Lower or upper regime planar lamination; low-angle cross-lamination; well-bedded.	Tabular–sharp to gradual base– 20 cm to 1 m.	Plant or carbonaceous debris; (BI=0-2), *Skolithos* isp.	Sedimentation from suspension in calm waters or under supercritical flow conditions; related to sedimentation on the surf or swash zones of beaches.
Spa	Whitish, medium-to-coarse-grained sandstones.	High-angle, planar cross-stratification; crude to well-bedded.	Sub-tabular–sharp and scoured bases–up to 4 m.	Null fossils; (BI=0-1), *Schacylindrichnus* isp.	Related to migration of straight-crested (2D) dunes or sand waves, and scroll bars.
St	Grey to greenish, fine-to-medium-grained sandstones.	Trough cross-lamination; medium-to-large-scale trough cross bedding; tangential-based cross lamination	Sub-tabular–sharp and planar contacts– 50 cm up to 4 m.	Some *Turritela* sp. and fragmented shells; (BI=1-2), *Macaronichnus* isp., *Planolites* isp.,	Related to migrating lunate or sinuous (3D) subaqueous dunes, modified by tides

		with mud drapes.		*Diplocraterion* ? isp.	forming epsilon cross-bedding. Large-scale migrating dunes are linked to prograding clinoforms.
Shb	Tan, fine- to medium-grained sandstones.	Bidirectional cross-bedding; herringbone cross-lamination; mud-drapes, and mud-partings.	Tabular–sharp contacts–30 cm to 90 cm.	Null fossils and bioturbation absent. Shell hash is common.	Related to migrating 2D-3D dunes products of the high-energy ebb and flood currents, whereas the mud represents irrupting slack water stages.
Gmm	Greyish to pale, (sub-) angular to sub-rounded pebbly to cobble conglomerates.	Sandy matrix-supported, structureless; large clasts up to 1m long.	Lenticular, tabular– sharp, erosive bases– 1 m up to11 m (amalgamated).	Shell hash, carbonaceous fragments, bioturbation absent.	Cohesive debris flow, hyperconcentrated sheet flood, generally high-shear strength preventing turbulence.
Gmg	Greyish to light brown, sub-angular to rounded, coarse to fine pebbly conglomerates.	Sandy clast- to matrix-supported, massive to normally graded, rare inverse grading.	Lenticular to subtabular– sharp, scoured bases; gradational top– up to 5 m.	Null fossils, carbonaceous fragments, bioturbation absent.	Winnowing of finer sediments forming a lag. Bed-load deposition from a diluted turbulent stream flow— inverse grading related to dispersive pressure on density-grain flows.
Gs	Greyish to dark-grey coarse shell-rich conglomerates.	Clast- (shell-) supported, normally graded shells; often massive.	Tabular to subtabular, lenticular– sharp contacts– up to 2m.	Oysters, bivalves, *Turritella* isp., and very fragmented shells; bioturbation absent.	Basal lag or shelly debris product of high-energy erosion and redeposition.

Palynomorphs	Taxa	Botanical affinity	Climate type
Epiphytic fungus (40.9%)	*Granatisporites* sp.	Uncertain	–
	Multicellaesporites sp.	Meliolaceae	
	Monoporisporites sp.		
Magnoliophytas (27.7%)	*Nothofagidites brassii* type	Dicotyledonae, Nothofagaceae, *Nothofagus*	CT
	N. dorotensis		
	N. cincta		
	N. diminuta		
	N. flemingii		
	N. spinosus	*Nothofagus betuloides*	
	Gaultheria sp.	Dicotyledoneae	WT
	Tricolpites sp.		
	Monocoplites sp.[ψ]	Monocotyledoneae	
Pteridophytas (21.4%)	*Laevigatosporites vulgaris*	Filicopsida, ?Blechnaceae	WT
	Cyathidites minor	Filicopsida, Cyatheaceae	
	Gleicheniidites sp.	Filicopsida, Gleicheniaceae	
	G. senonicus	*Gleichenia circinata*	
	Clavifera triplex	*Dicranopteris rigida*	
	Lycopodium austroclavidites	Lycopodiaceae, *Lycopodium*	
	Polypodiisporites sp.	Uncertain	
Pinophytes (7%)	*Podocarpidites otagoensis*	Podocarpaceae, *Podocarpus*	CT
	P. marwickii	*Podocarpus salignus*	
	Araucariacites australis	Araucariaceae (*Araucaria*)	
Microalgae colonies (3%)	*Botryococcus braunii*	Chlorophyta, Chlorococcales, Botryococcaceae	–
Minor dinocysts	*Spiniferites* sp.	Dinoflagellata	–

[ψ] Representing 10.2% from the overall Magnoliophytas identified; CT=cool temperate; WT=warm temperate

HIGHLIGHTS

- Flexural and dynamic subsidence originated the Maastrichtian-Danian transgression.
- Estuarine deposits and deep-water turbidites represent the transgression.
- Hinterland exhumation and stalled deformation front during the Maastrichtian.
- Significant forelandward advance of the deformation front by the Paleocene.

Figure 1

Click here to download high resolution image

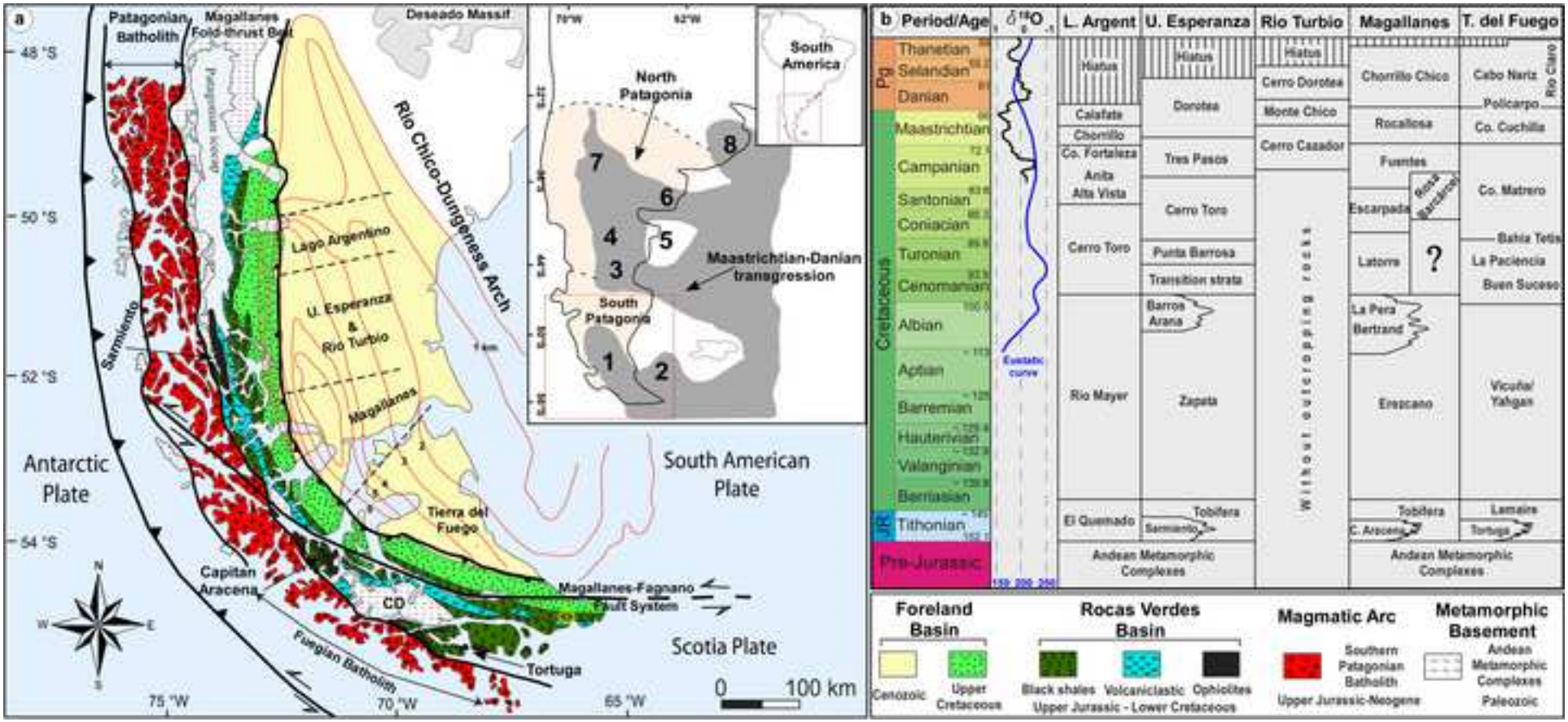

Figure 2

Click here to download high resolution image

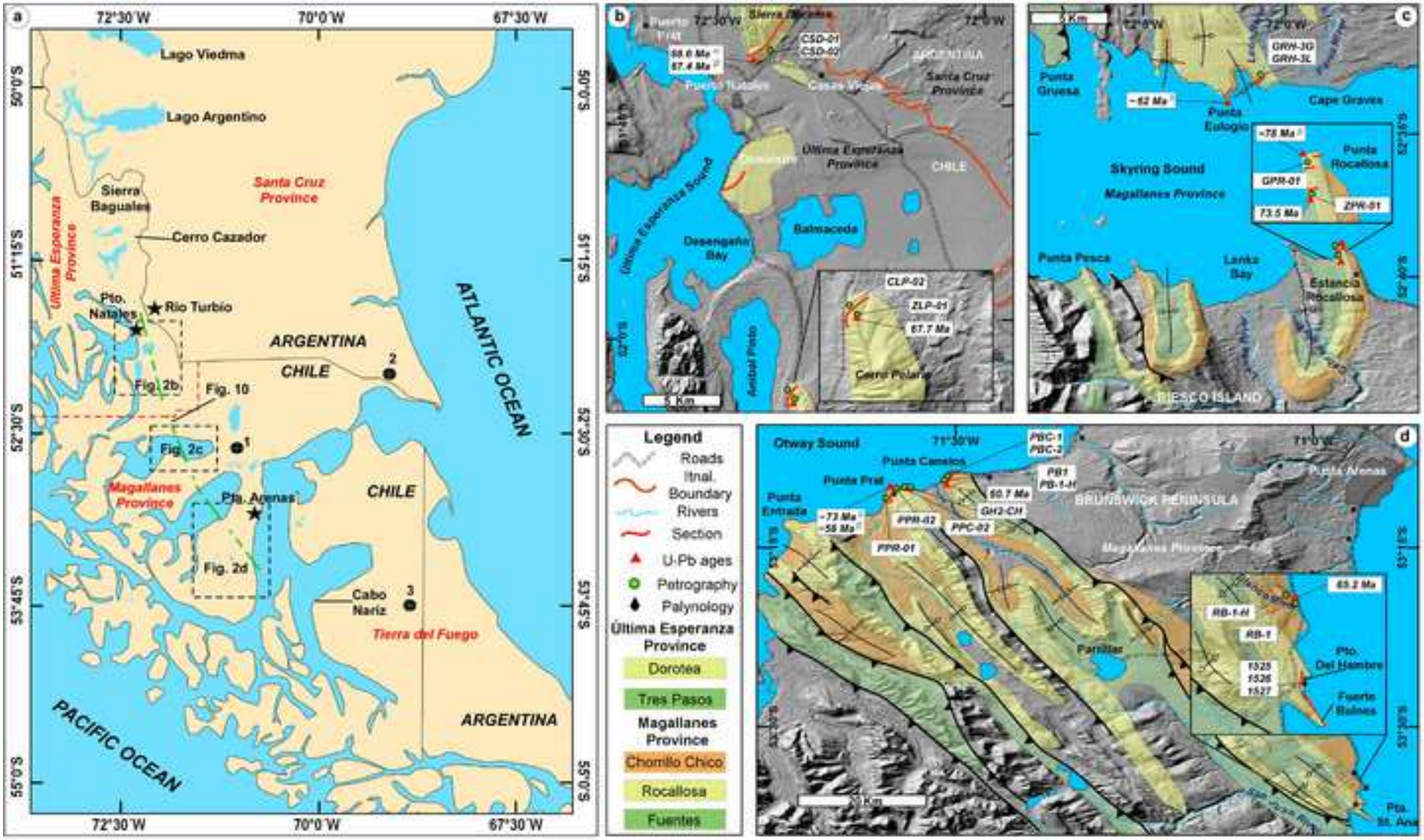

Figure 3a

Click here to download high resolution image

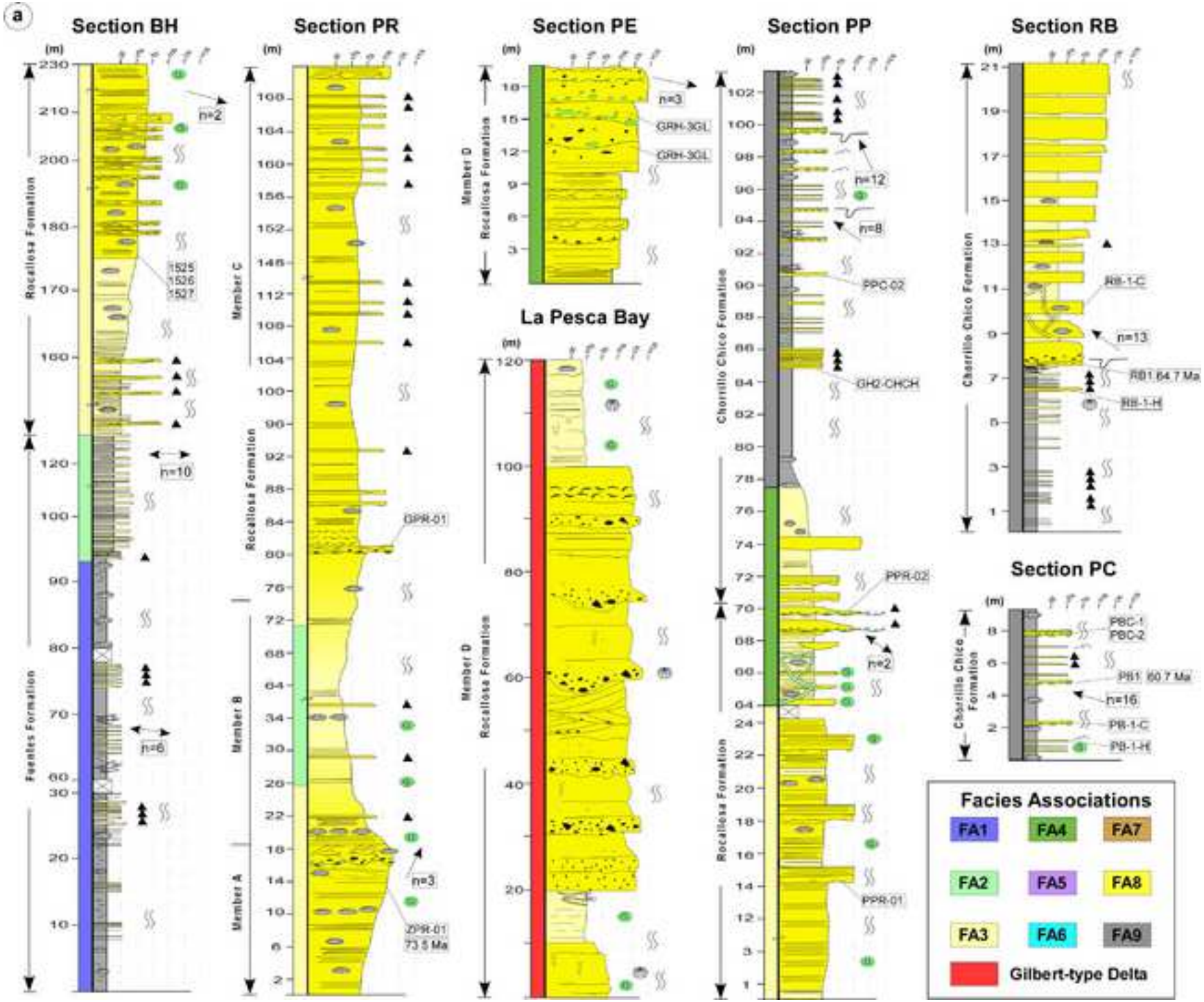

Figure 3b

Click here to download high resolution image

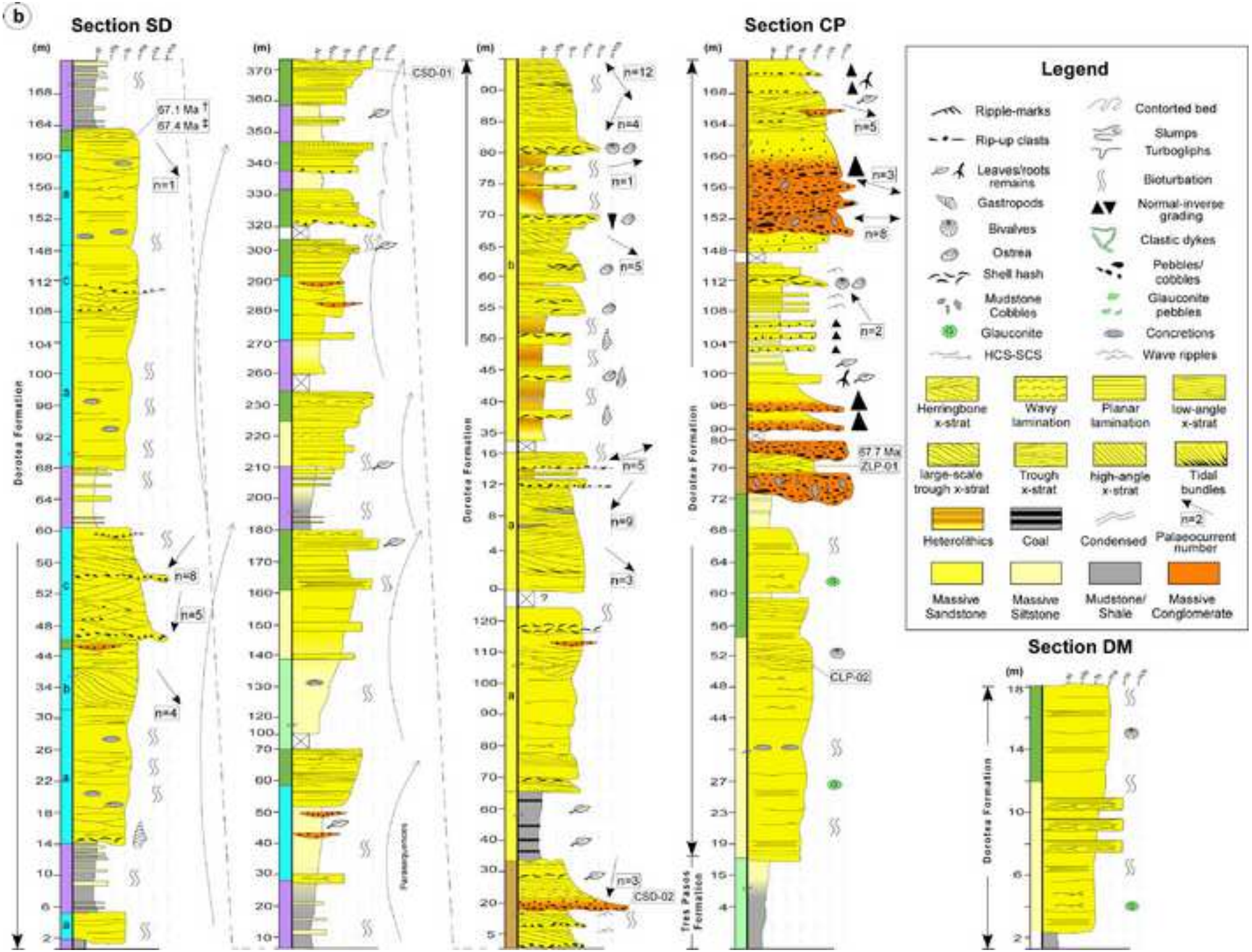

Figure 4

Click here to download high resolution image

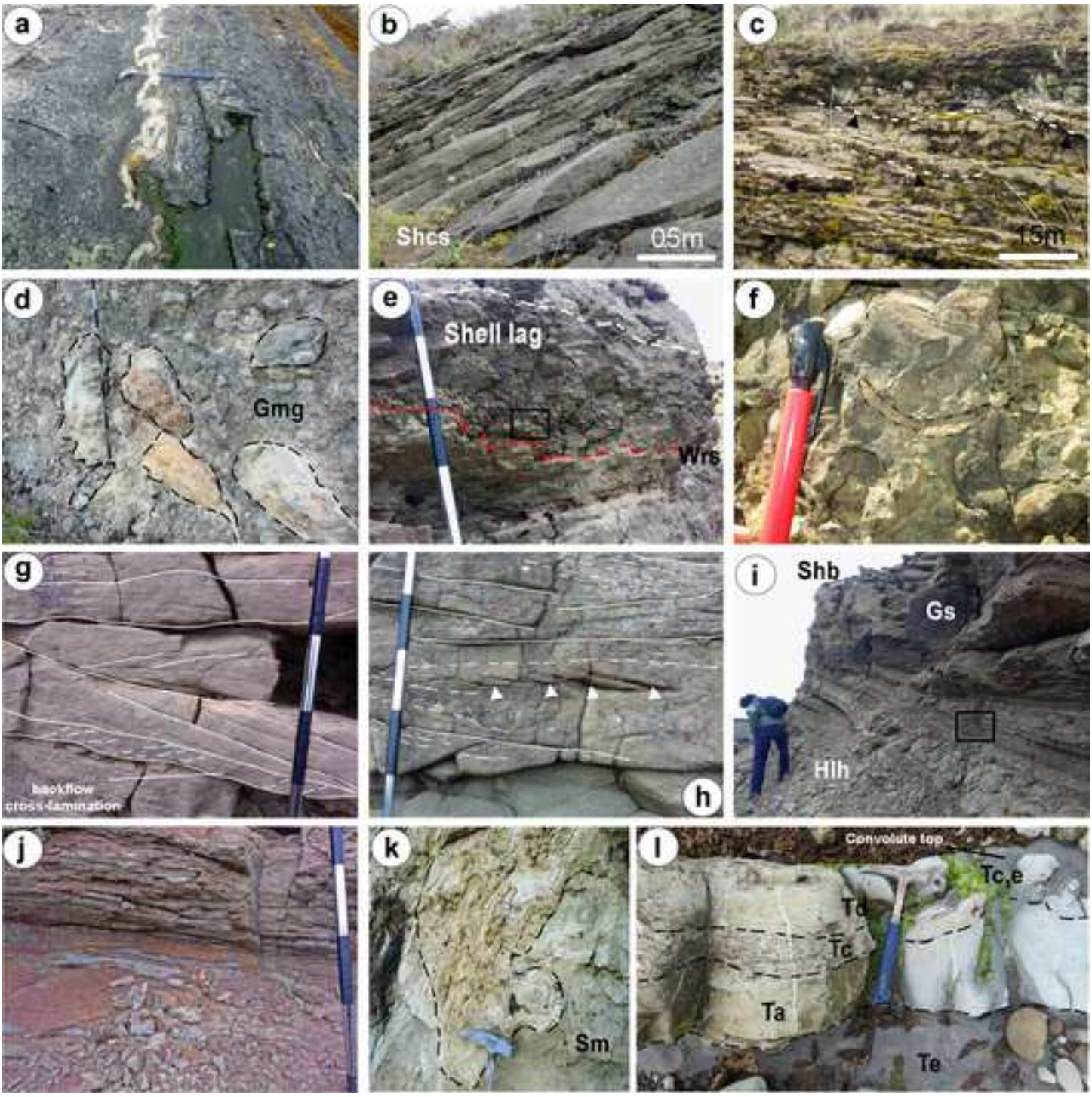

Figure 5

Click here to download high resolution image

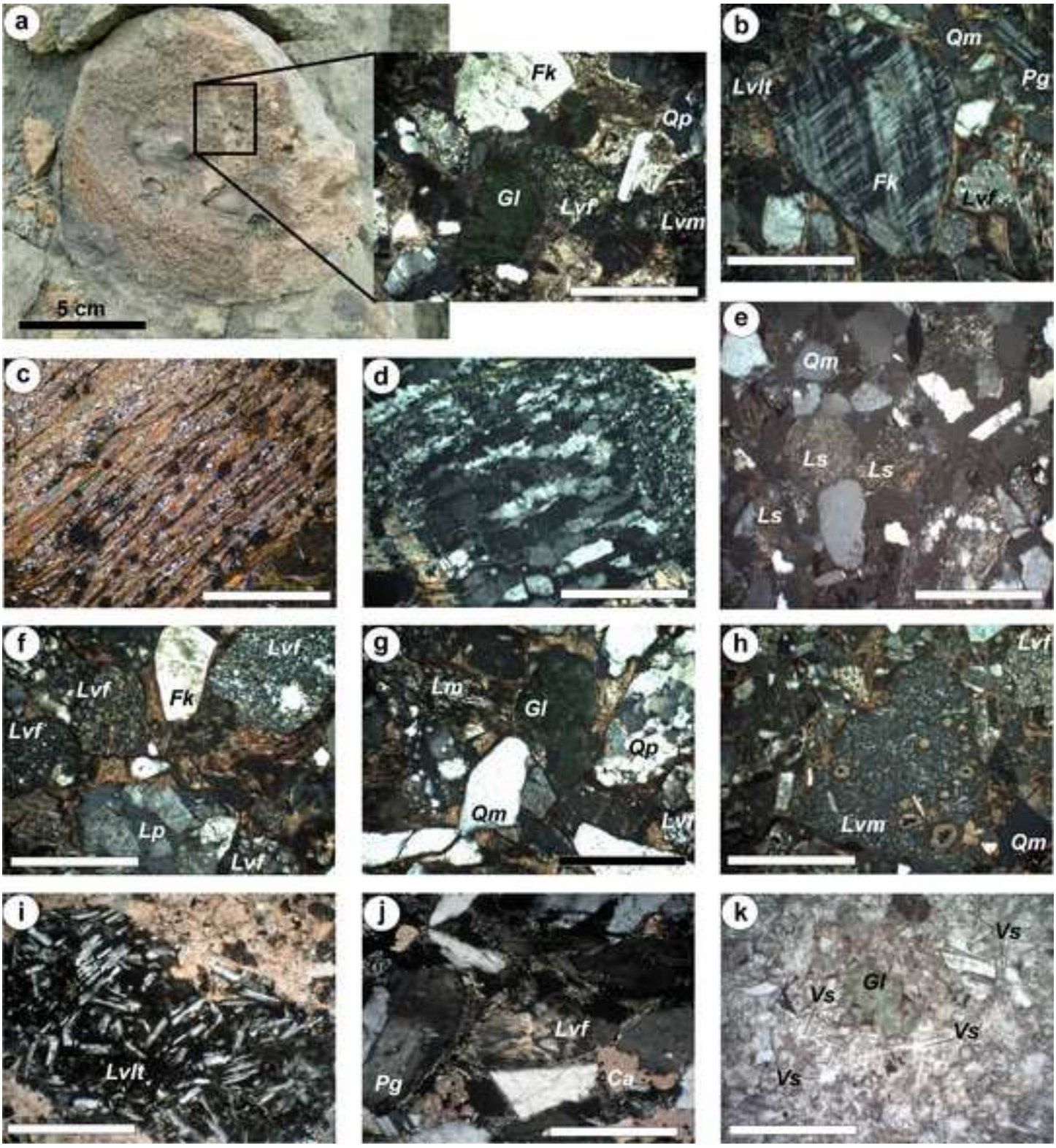

Figure 6

Click here to download high resolution image

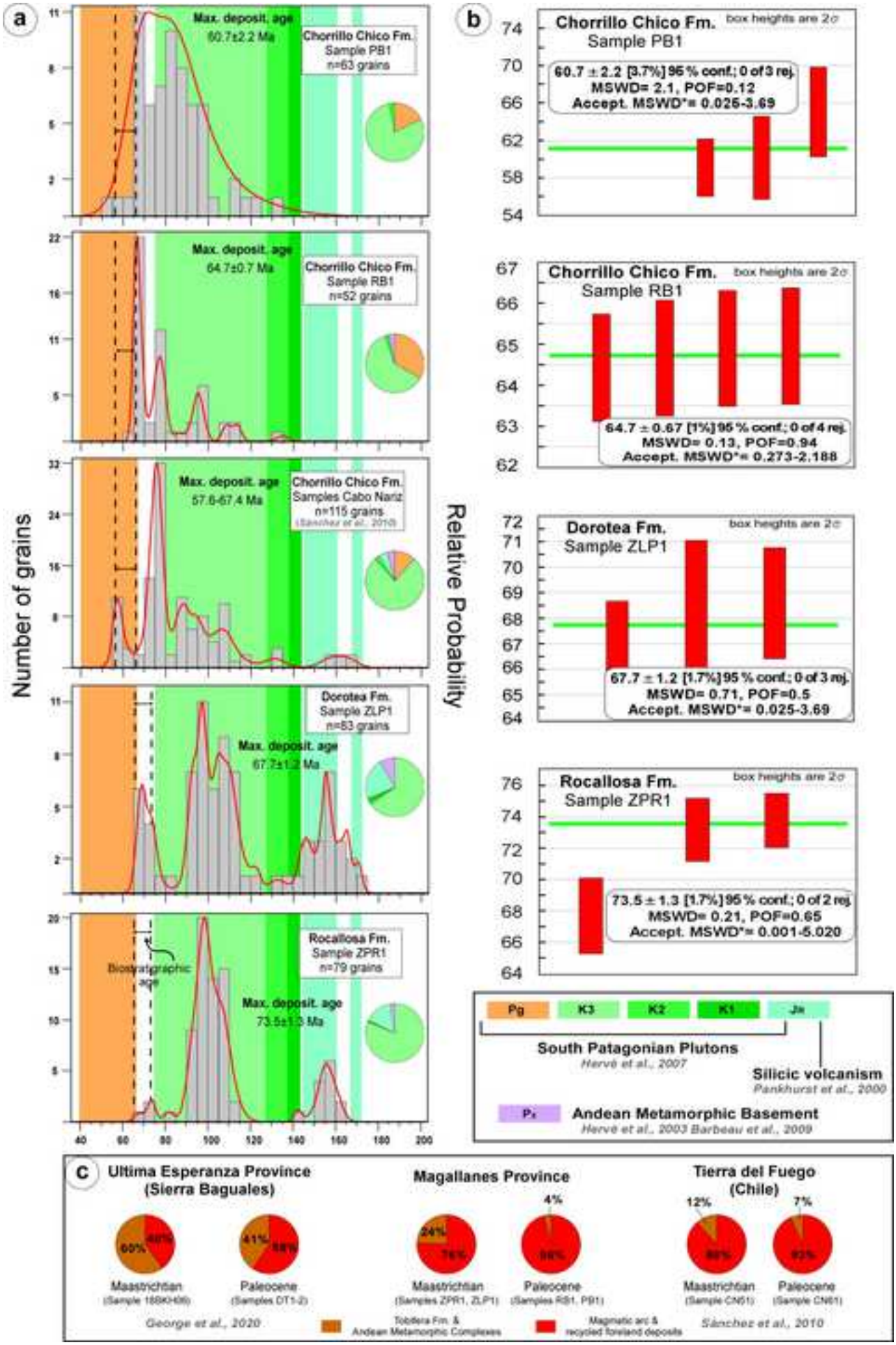

Figure 7

Click here to download high resolution image

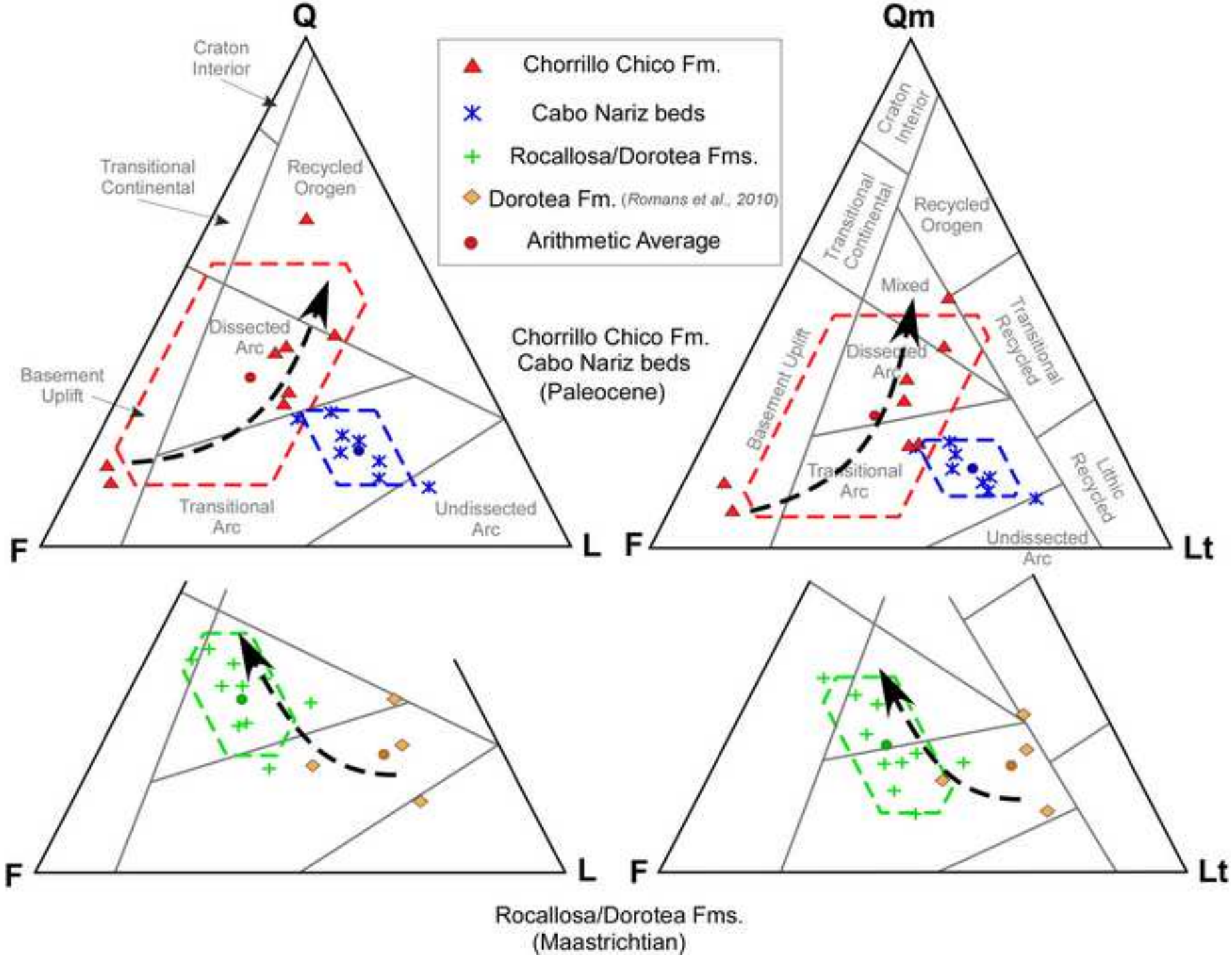

Figure 8

Click here to download high resolution image

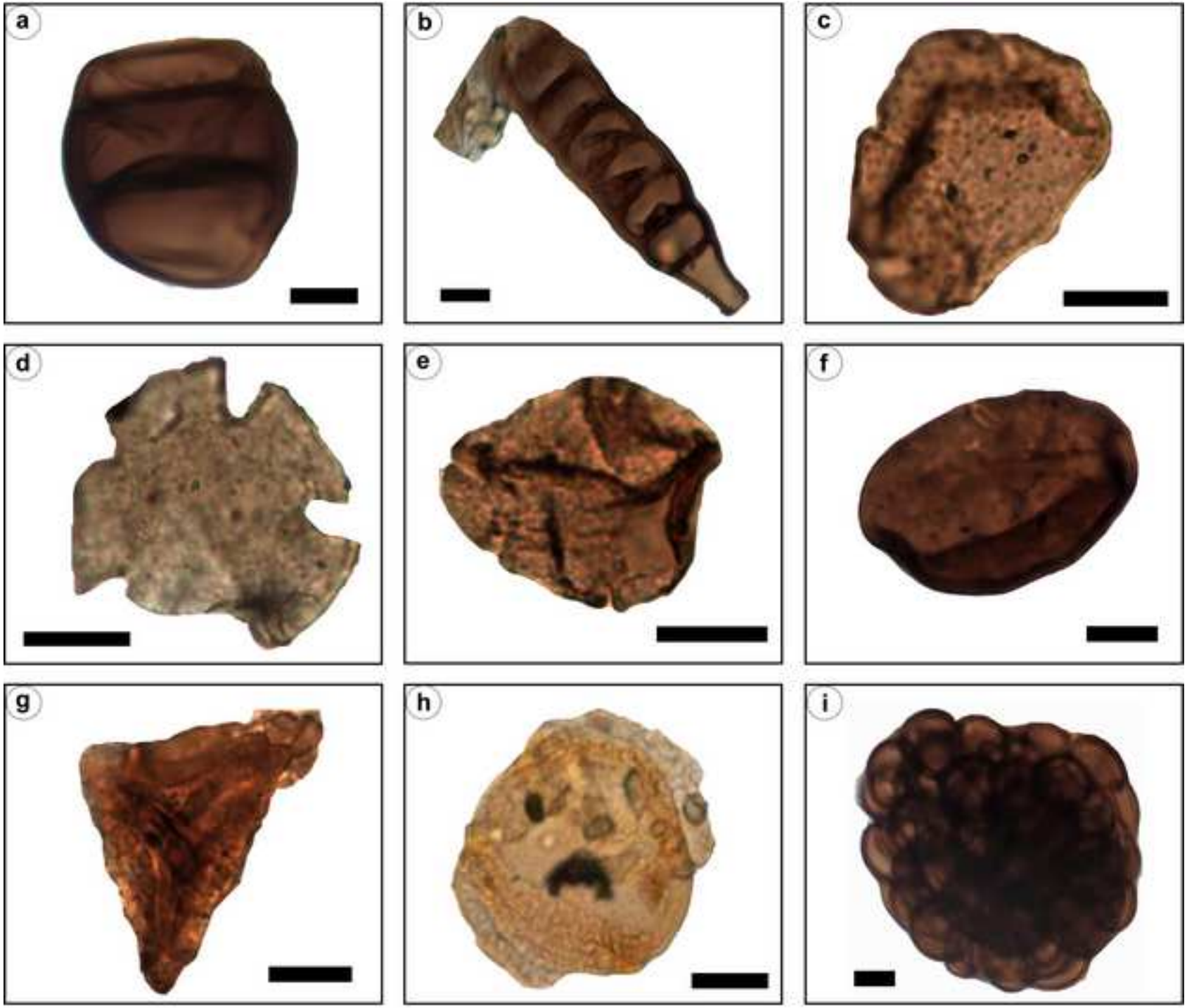

Figure 9

Click here to download high resolution image

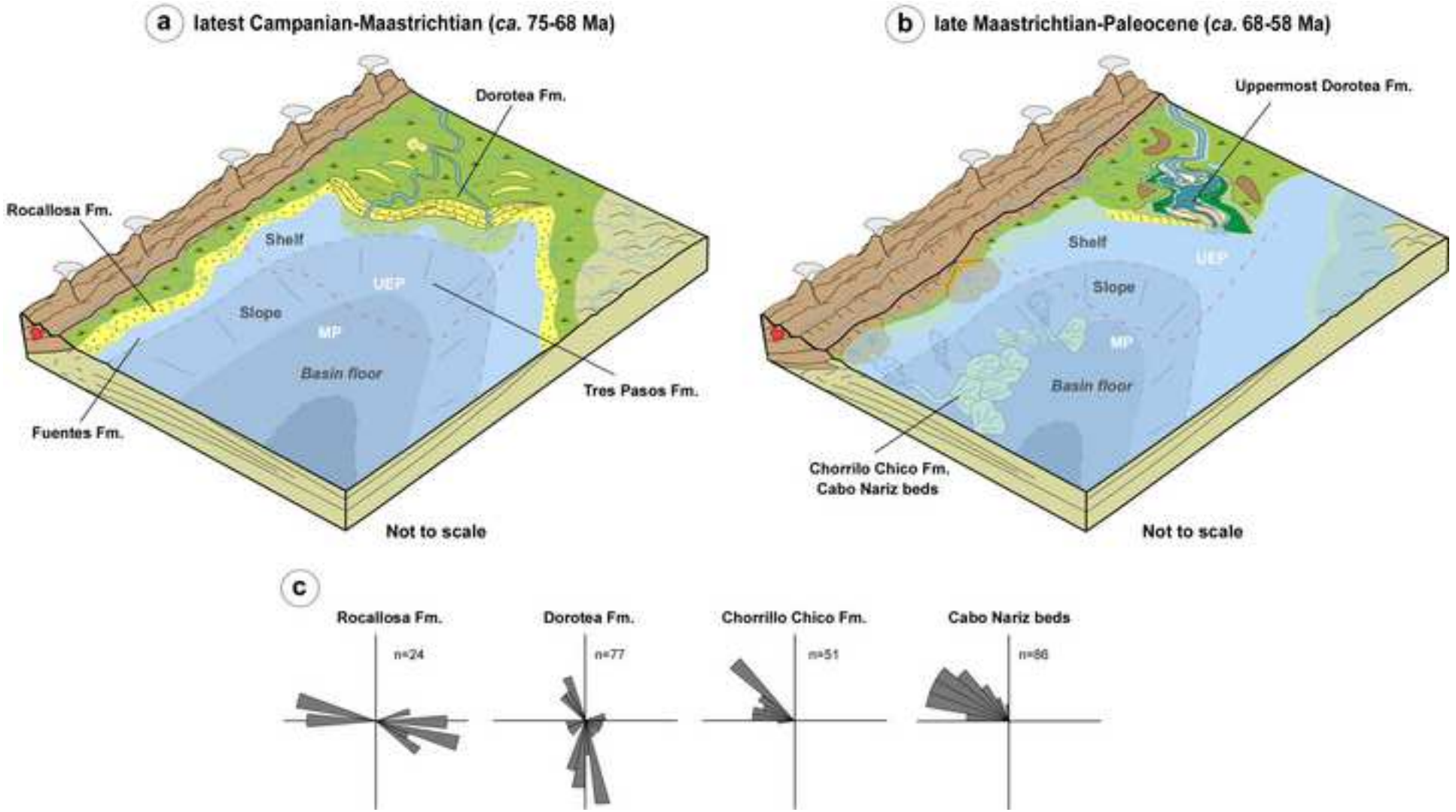

Figure 10

Click here to download high resolution image

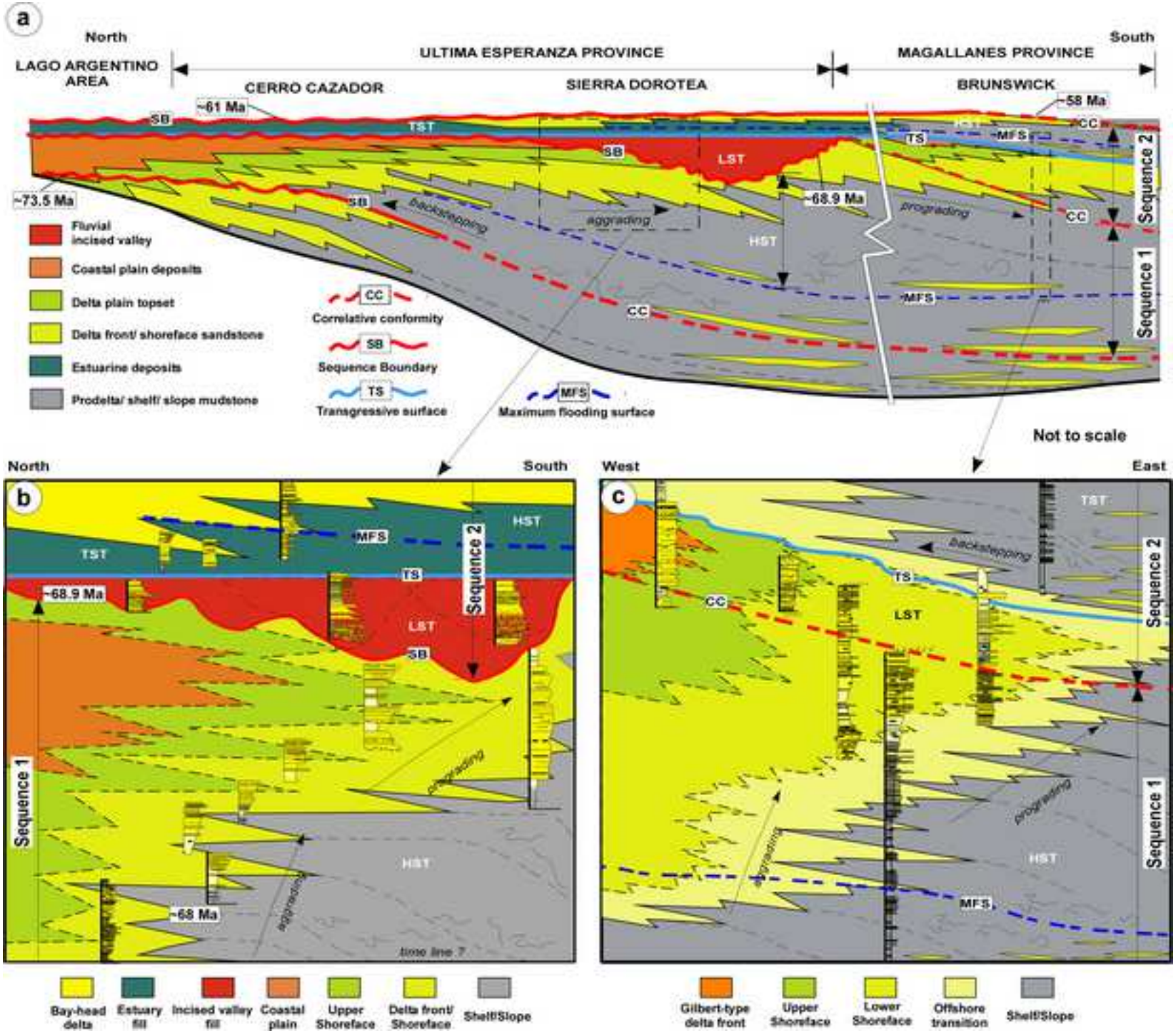

Figure 11
Click here to download high resolution image

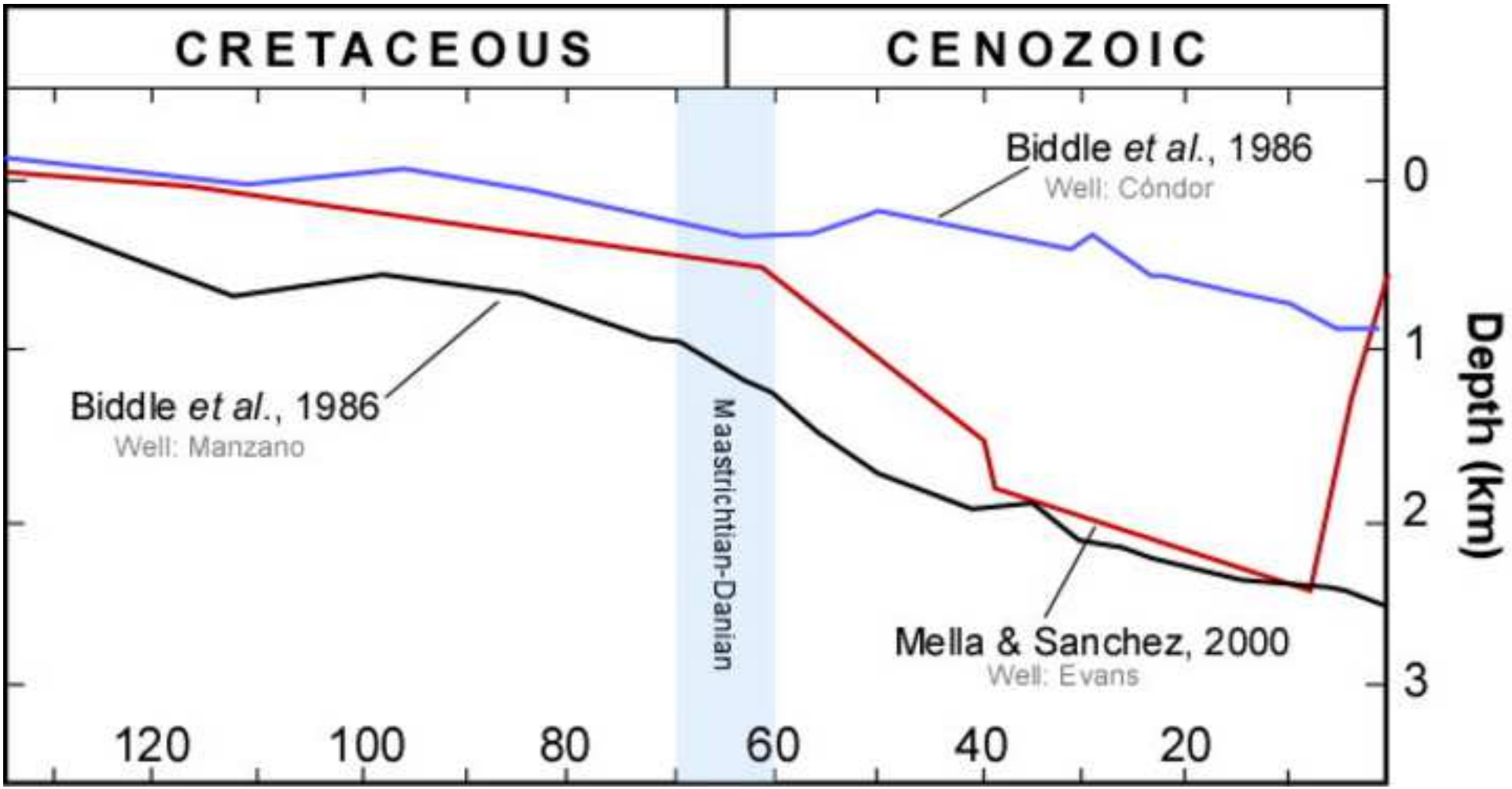

Figure 12

Click here to download high resolution image